

# A wet heterogeneous mantle creates a habitable world in the Hadean

<https://doi.org/10.1038/s41586-021-04371-9>

Yoshinori Miyazaki<sup>1,2</sup>✉ & Jun Korenaga<sup>1</sup>

Received: 3 August 2020

Accepted: 20 December 2021

Published online: 2 March 2022

 Check for updates

The Hadean eon, following the global-scale melting of the mantle<sup>1–3</sup>, is expected to be a dynamic period, during which Earth experienced vastly different conditions. Geologic records, however, suggest that the surface environment of Earth was already similar to the present by the middle of the Hadean<sup>4,5</sup>. Under what conditions a harsh surface environment could turn into a habitable one remains uncertain<sup>6</sup>. Here we show that a hydrated mantle with small-scale chemical heterogeneity, created as a result of magma ocean solidification, is the key to ocean formation, the onset of plate tectonics and the rapid removal of greenhouse gases, which are all essential to create a habitable environment on terrestrial planets. When the mantle is wet and dominated by high-magnesium pyroxenites, the removal of carbon dioxide from the atmosphere is expected to be more than ten times faster than the case of a pyrolytic homogeneous mantle and could be completed within 160 million years. Such a chemically heterogeneous mantle would also produce oceanic crust rich in olivine, which is reactive with ocean water and promotes serpentinization. Therefore, conditions similar to the Lost City hydrothermal field<sup>7–9</sup> may have existed globally in the Hadean seafloor.

The Hadean Earth is often viewed as an uninhabitable world with a partially molten surface, active volcanism and a hot steamy atmosphere. The picture of harsh surface conditions may be expected from the Moon-forming giant impact<sup>1,2</sup> and the subsequent bombardment by leftover planetesimals<sup>10</sup>, but ancient geological records suggest that by approximately 4.3 Gyr ago (Ga), the Earth's surface had become similar to the present-day environment with oceans and granitic crust<sup>4,5</sup>. Hadean detrital zircons, enriched in heavy oxygen and yielding low melting temperatures, indicate that liquid water was already present at the Earth's surface. Furthermore, by the end of the Hadean, the global carbon cycle is likely to have stabilized the climate and maintained a surface temperature similar to the present day<sup>11</sup>. The first 500 Myr of our planet, therefore, should have experienced a dramatic change in the climate, evolving quickly from being uninhabitable to habitable.

The troposphere during the early Hadean is believed to comprise greenhouse gases released during the solidification of a magma ocean<sup>12–16</sup>. The composition and redox state of the early atmosphere have been a subject of discussion<sup>17,18</sup>, but Earth is expected to have had a thick atmosphere of CO<sub>2</sub> and H<sub>2</sub>O, which maintained an extreme climate on the early Earth<sup>13,19</sup>. To create a habitable environment within the Hadean period, most of the greenhouse gases must be removed from the atmosphere within the same timescale. Indeed, the atmospheric pressure of CO<sub>2</sub> is estimated to have been lower than 1 bar at the end of the Hadean<sup>11,20</sup>. CO<sub>2</sub>, the major constituent of greenhouse gases, can be sequestered into the Earth's interior by being transformed into carbonate minerals at ocean basins, and then subducted to the mantle<sup>6</sup>. It remains unclear, however, whether the sequestration was efficient enough to produce a habitable environment by 4.0 Ga. In this study, this question is addressed by delineating the mode of geodynamics during the Hadean. We first investigate the efficiency of mantle degassing

during the solidification of a magma ocean, which is crucial for constraining the degree of hydration and thus the rheology of the Hadean mantle. We then turn to quantify the surface renewal rate and examine the rate of carbon sequestration.

## Inefficient degassing of a magma ocean

First of all, an efficient degassing of the mantle is unlikely during the solidification of a magma ocean if a rheological transition in a partially molten medium is taken into account. A magma ocean behaves rheologically as solid when the melt fraction becomes lower than a certain threshold (a typical value assumed in magma ocean studies is 40%)<sup>19,21</sup>, and if percolation is not rapid enough, volatiles would be trapped in the porous melt phase<sup>22</sup>. Volatiles, in particular water, would remain dissolved in the melt phase until the melt fraction becomes lower than 0.2 wt%. Melt can contain water by more than 50 wt% at high pressures<sup>23,24</sup>, and the initial water mantle inventory is estimated to be 0.04–0.1 wt%<sup>25,26</sup>. Furthermore, the newly formed solid matrix would be continuously transported downwards by the Rayleigh–Taylor instability<sup>27,28</sup>, and because the downwelling velocity of the instability is faster than melt percolation<sup>21</sup>, volatiles would be sequestered in the deep mantle. Therefore, water would either be trapped in the solid matrix as bubbles or would diffuse into the surrounding nominally anhydrous minerals. This indicates that a large fraction of water would remain in the mantle even after the solidification (Fig. 1). If volatiles, behaving as incompatible elements, concentrate at the surface melt layer as magma ocean solidifies from the bottom to the top<sup>12–14</sup>, volatile concentrations eventually exceed saturation levels, but such a high concentration of volatiles would not be reached if the rheological transition is taken into account.

<sup>1</sup>Department of Earth and Planetary Sciences, Yale University, New Haven, CT, USA. <sup>2</sup>Division of Geological and Planetary Sciences, California Institute of Technology, Pasadena, CA, USA.

✉e-mail: ymiya@caltech.edu

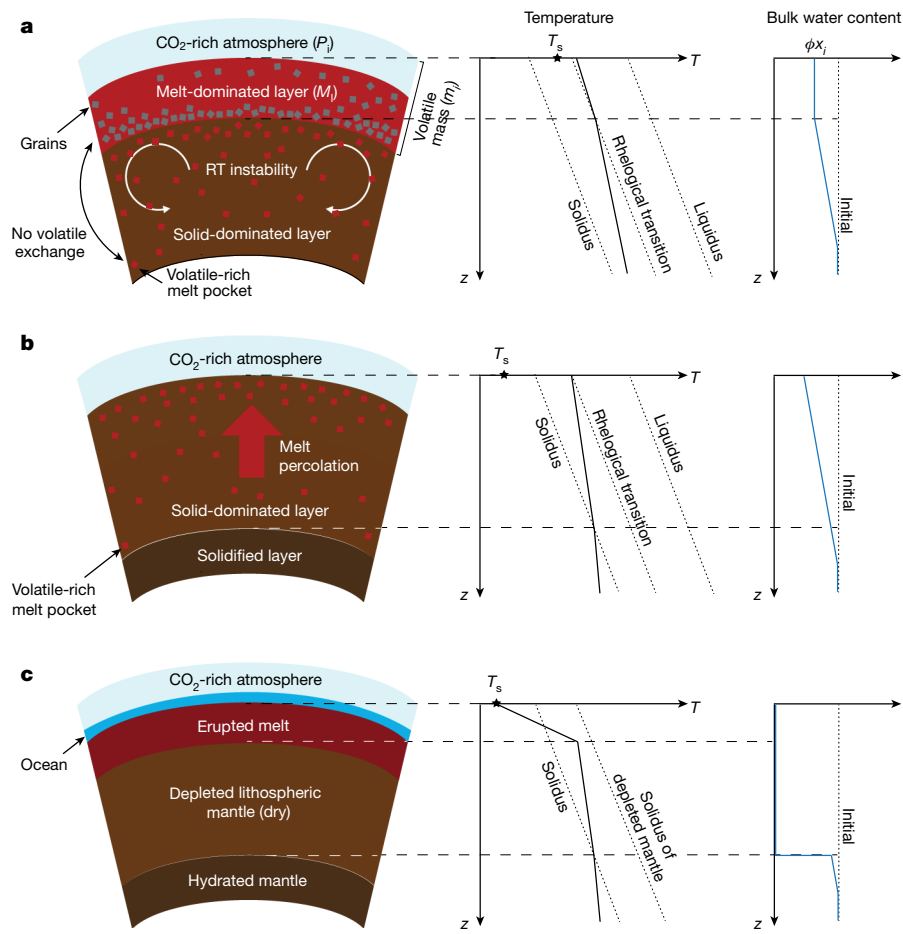


**Fig. 1 | Schematic illustration of how a magma ocean solidifies with the evolution of atmosphere.** Only the shallow mantle is illustrated here. **a**, A magma ocean solidifies from the bottom, and the porous melt phase emerges in regions where melt fraction falls below a critical value. Volatiles in the deep mantle are stored in such a residual melt phase instead of being concentrated near the surface. Note that a magma ocean has two rheologically distinct layers, the melt-dominated and solid-dominated. The former is mixed by rapid convection, whereas the latter is mixed by the Rayleigh–Taylor (RT) instability, both creating an adiabatic thermal profile. Parameters used in equation (1) (Methods) are labelled to corresponding reservoirs. **b**, When the

melt-dominated layer diminishes, convective heat flux plummets, and the surface temperature (star) drops below the mantle solidus. Melt percolation governs the subsequent evolution because solid-state convection is slow. **c**, Erupted melt from the residual melt phase forms a solidified lid, leaving a depleted dry mantle behind. By releasing dissolved volatiles to the atmosphere, the atmosphere contains enough amount of volatile to form oceans on a cooled surface. The deeper region of the mantle is completely solidified and thus would not degas by percolation. Although it is not shown here, the deeper region contains small-scale iron-rich blobs because we consider a chemically heterogeneous mantle in this study (Fig. 3a).

The mass of atmosphere degassed from a magma ocean, therefore, is expected to be smaller than that predicted in refs.<sup>12–16</sup>. With this effect of rheological transition on degassing<sup>22</sup>, we predict the evolution of atmospheric mass during magma ocean solidification using volatile partitioning between the atmosphere and the surface of a magma ocean. Because the solubilities of volatiles increase with pressure, those at the surface govern the volatile budget of the mantle. Figure 2a illustrates that although approximately 80% of the total carbon inventory would reside in the atmosphere, about 99% of water would remain in the mantle. Here we assume that the mantle contained between 0.04 and 0.1 wt% of H<sub>2</sub>O (corresponding to approximately 1.2 and 3 ocean mass, respectively) and 200–500 parts per million (ppm) of CO<sub>2</sub>, based on estimates for the present-day volatiles budget<sup>25,26</sup>. We find that the atmospheric pressure of volatiles is mostly constant during the evolution because, when volatiles are trapped in the porous melt phase, the solidification process has a negligible effect on volatile concentration in the magma ocean. The atmospheric pressure increases by a small degree during the final stage of solidification as surface magma starts to solidify and volatiles become enriched in the melt phase (Fig. 2a).

Even so, with an initial water inventory of 1.2 ocean, the surface water is limited to about 0.011 ocean mass with a partial pressure of 7 bar (Fig. 2a). On the other hand, a large fraction of CO<sub>2</sub> would be degassed to the atmosphere from the beginning of the evolution because CO<sub>2</sub> is less soluble than H<sub>2</sub>O in silicate melt<sup>22,15</sup>. Our partitioning model predicts that the partial pressure of CO<sub>2</sub> would be approximately 110 and 290 bar with initial concentrations of 200 and 500 ppm, respectively. Surface water would be supplemented by another degassing after the disappearance of the melt-dominated layer. When the surface of a magma ocean behaves rheologically as liquid (Fig. 1a), high convective heat flux, supported by low melt viscosity, maintains a high surface temperature above 1,000 °C (Fig. 2b)<sup>13,15</sup>. When cooling proceeds and the surface becomes rheologically solid (Fig. 1b), however, convective heat flux decreases by orders of magnitude, and a one-dimensional (1D) atmospheric model suggests that the surface temperature drops discontinuously to a temperature below the mantle solidus. At this point, the Rayleigh–Taylor instability, which can happen rapidly and frequently<sup>28</sup>, should have cooled the mantle, changing the mantle thermal structure to be adiabatic from superadiabatic, and solid-state

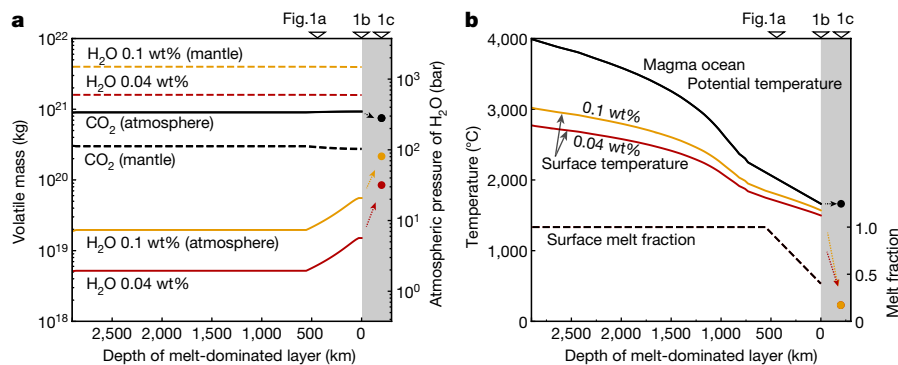


**Fig. 2 | Mantle degassing considering the effect of the rheological transition.** Figures are shown as a function of the depth of a melt-dominated layer, and the system evolves from left to right as solidification proceeds. **a**, The volatile budgets of H<sub>2</sub>O (coloured) and CO<sub>2</sub> (black) in the atmosphere (solid) and the mantle (dashed). **b**, Surface temperature (coloured), the potential temperature of magma ocean (black), and the surface melt fraction (dashed). The corresponding atmospheric pressures of H<sub>2</sub>O are shown in the

convection would govern the cooling thereafter<sup>21,30</sup>. Timescale comparison suggests that solid-state convection is slower than upward melt percolation in the upper mantle (see Methods), so residual melt in the shallow upper mantle would percolate upward and erupt to the surface. On the basis of a mantle melting model, we predict that the top 4 GPa of the upper mantle (Fig. 1b, Extended Data Fig. 1a) was partially molten at the beginning of solid-state convection, and volatiles in this layer were extracted to the atmosphere. For the case of 0.04 wt% initial water content, a total of about 0.06 ocean mass of water is released to the atmosphere, creating approximately 36 atm of water vapour atmosphere (Fig. 2a, Extended Data Table 1). This exceeds a threshold of 0.05 ocean mass to form water oceans when the atmosphere contains 200 bar of CO<sub>2</sub><sup>19</sup>, so the presence of ocean is plausible immediately after the solidification of a magma ocean. The surface temperature exceeds 100 °C owing to the greenhouse effect, yet liquid water is stabilized by high atmospheric pressure. At the same time, the mantle would still contain a large fraction of water and is expected to be hydrated, lowering the viscosity<sup>31,32</sup> of the Hadean mantle.

### Rapid plate motion of a wet heterogeneous mantle

We now turn to the second question of carbon sequestration. With the presence of oceans, the operation of plate tectonics is theoretically possible even in the early Hadean<sup>33,34</sup>, so CO<sub>2</sub> could be removed by the formation and subduction of carbonate minerals. The partial pressure of CO<sub>2</sub> is estimated to have been below 1 bar by the end of the Hadean<sup>11,20</sup>, so greater than 100 bar of CO<sub>2</sub> has to be transported back into the mantle. The frequent renewal of the surface by rapid cooling has been proposed as a possible mechanism<sup>6,35</sup>, but, contrary to a common belief, a hotter mantle in the past points to more sluggish plate motion because of thicker depleted lithospheric mantle<sup>33,36</sup>. Slow plate motion of a hotter mantle, in fact, is corroborated by a range of geological records<sup>37–39</sup>. Moreover, the Hadean mantle could have been chemically stratified as a result of an overturn after the solidification of magma ocean, with iron-rich dense materials at the bottom<sup>12</sup>. If so, the mantle would be resistant to thermal convection<sup>40</sup>, and plate motion would be even slower, if not totally absent. A hotter mantle in the Hadean, therefore, does not necessarily indicate the rapid sequestration of CO<sub>2</sub>.

We propose that rapid recycling is possible with a chemically heterogeneous mantle, which results from the fractional crystallization of a magma ocean<sup>28</sup>. The differentiation of a magma ocean is driven by the settling and sedimentation of a liquidus mineral, bridgmanite, at the base of the melt-dominated layer. Consequently, high-Mg# (defined as

right axis). The H<sub>2</sub>O contents are coded by colour as 0.04 (red) and 0.1 (yellow), corresponding to 1.2 and 3 ocean mass, respectively. Here, the initial CO<sub>2</sub> concentration in the mantle is set to 300 ppm. Dots in shaded regions indicate the state after the complete solidification as described in Fig. 1c. For concentrations in the mantle, values after the complete solidification are not shown because only the uppermost layer is affected by melt percolation, and volatiles concentrations in the deeper region remain unchanged.

molar Mg/(Mg + Fe) × 100) and SiO<sub>2</sub>-rich materials would constitute the lower mantle, whereas the upper mantle would be comprised of residual iron-rich dense materials (Fig. 3a). Our scaling analysis suggests that such a gravitationally unstable structure is subject to small-scale Rayleigh–Taylor instabilities with a length scale shorter than 100 km<sup>28</sup>. At the end of solidification, iron-rich materials would thus have existed as small blobs embedded in a high-Mg# pyroxenite matrix (Fig. 3a). As explained in detail later, such a mantle with small-scale heterogeneity would not develop thick depleted lithospheric mantle, so rapid plate motion and efficient carbon sequestration could be achieved. In the following, we estimate the surface evolution timescales for both homogeneous and heterogeneous mantles. Our results suggest that the chemically heterogeneous mantle is more compatible with creating a habitable environment by the end of the Hadean.

The chemically heterogeneous mantle is predicted to experience limited dehydration at mid-ocean ridges. Modelling of magma ocean solidification suggests that the pyroxenite matrix has an average Mg# of 94 and constitutes approximately 75% of the mantle<sup>28</sup>. The high-Mg# pyroxenite yields a higher solidus than a homogeneous pyrolytic mantle, and with a mantle potential temperature of 1,600 °C, the Rhyolite-MELTS and pMELTS models<sup>41,42</sup> predict that the initial depth of melting is about 4 GPa with 0.1 wt% of water (Extended Data Fig. 1a). As the mantle undergoes fractional melting, the pyroxenite matrix becomes mostly dehydrated at approximately 2 GPa and forms a depleted lithospheric mantle of 40-km thickness (Extended Data Fig. 1b). Iron-rich blobs would also melt during their upwelling, but because they are of small scale, their melting would not contribute to producing a uniformly thick depleted lithospheric mantle. Stress necessary to bend plates is smaller with thinner depleted lithospheric mantle, whereas stress due to the negative buoyancy of plates increases under a higher potential temperature, so the operation of plate tectonics is plausible (see Methods). Pyrolyte, on the other hand, starts to melt at a depth deeper than 10 GPa, and because it is rich in olivine, which is less compatible with water than pyroxene, a pyrolytic mantle would dehydrate faster than pyroxenite. Crust and depleted lithospheric mantle are thus estimated to be as thick as about 26 km and 145 km, respectively, at a mantle temperature 250 K hotter than that of the present day (Fig. 3b, Extended Data Fig. 2).

Thin depleted lithospheric mantle is key for rapid plate motion under a hotter mantle. Because the depleted lithospheric mantle is drier and thus stiffer, thicker lithosphere results in slower convection than the present-day mantle<sup>43</sup> (Fig. 3c). Also, the presence of thick buoyant crust would require a longer cooling time for plate to be negatively

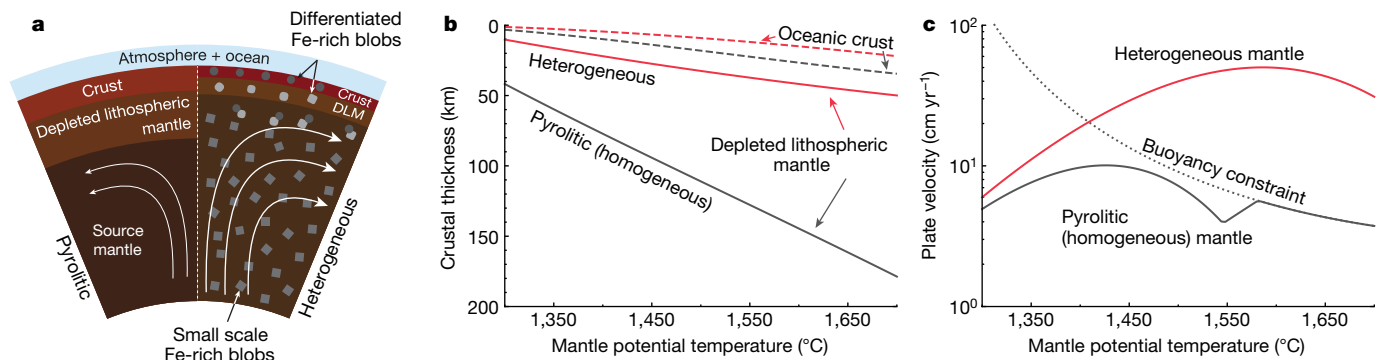


**Fig. 3 | Crustal thickness and plate velocity of chemically heterogeneous and pyrolitic (homogeneous) mantles.** **a**, Schematic illustration of the near-surface structure for pyrolitic (left) and chemically heterogeneous (right) mantles. **b**, Estimated thicknesses of oceanic crust (dashed) and depleted lithospheric mantle (solid lines) for different mantle potential temperatures. Colour indicates chemically heterogeneous (red) and pyrolitic homogeneous mantles (grey). **c**, Plate velocities for different mantle potential temperatures.

A stiff depleted lithospheric mantle is thicker for a pyrolitic homogeneous mantle, resulting in more sluggish plate motion for a hotter mantle. The plate velocity of a mantle hotter than 1,590 °C would be further limited by a buoyancy constraint (dotted). With thicker oceanic crust, a longer cooling time or a thicker thermal boundary layer is required for plate to be negatively buoyant. A mantle water content of 0.1 wt% is assumed here.

buoyant<sup>44</sup>, which would further limit the plate velocity. The scaling of plate tectonic convection<sup>45</sup> suggests that, for a pyrolitic mantle, average plate velocity would remain the same as the present at a potential temperature of 1,600 °C. By contrast, the depleted lithospheric mantle of chemically heterogeneous mantle is thin enough to allow for rapid plate motion, and its crust is only marginally chemically buoyant because of crust produced from iron-rich blobs, which has a density greater than 3,500 kg m<sup>-3</sup> (Extended Data Table 2), and would help to negate the chemical buoyancy of oceanic crust. Plate velocity for the heterogeneous mantle is estimated to be approximately 50 cm yr<sup>-1</sup> (Fig. 3c), and ocean basins would be renewed around every 9 Myr, allowing the rapid recycling of carbonate minerals. It is noted that, if the mantle had degassed completely during magma ocean solidification, the whole mantle would be dry and stiff, and its viscosity would be about 50 times higher than that of the present-day mantle, even considering the effect of a higher temperature<sup>31,32</sup>. Plate velocity would be limited to approximately 2 cm yr<sup>-1</sup> (see Methods), and the surface renewal rate becomes smaller than that of a pyrolitic mantle.

Furthermore, the Hadean seafloor could store a greater amount of carbonate minerals because seawater circulating through oceanic crust has a higher CO<sub>2</sub> content. The solubility of CO<sub>2</sub> under 100 bar is higher by at least an order of magnitude than the present-day atmosphere<sup>46</sup>, and thus the alteration of upper oceanic crust is expected to have been considerable. When Ca and Mg in the top 500 m of the crust, a layer with high porosity, were used to form carbonates, an equivalent of around 22 bar could be stored to the mantle, which is nine times larger

than the present-day value of 2.5 bar<sup>47</sup>. The *P-T* path of the Hadean slab would resemble the present-day young subduction zones (Extended Data Fig. 3), so some fraction of carbonates may melt and return to the surface. Yet, even assuming that half of subducted carbonates are recycled, 200 bar of CO<sub>2</sub> could be removed from the atmosphere within 160 Myr (Fig. 4). By contrast, if the mantle were pyrolitic, sluggish plate motion would limit the sequestration of CO<sub>2</sub>. Our model predicts that the atmospheric CO<sub>2</sub> remains higher than 10 bar with a surface temperature over 100 °C for 1.5 Gyr (Fig. 4), which fails to explain the evolution of Earth's atmosphere and surface conditions. If the mantle was pyrolitic in the Hadean, the removal of CO<sub>2</sub> from the atmosphere is unlikely to be completed until the mid-Archean.

A high iron-rich olivine content in crust of the chemically heterogeneous mantle (Extended Data Table 2) would promote serpentinization reactions<sup>48</sup>, which has an important implication for the earliest life on Earth<sup>49</sup>. Serpentinization releases hydrogen and methane by reducing water (Fig. 4a), and the anaerobic oxidation of methane is considered to have supported nascent life forms before the beginning of photosynthesis. Methane released by seafloor serpentinization is also observed now at the Lost City hydrothermal field (LCHF)<sup>7</sup> located along the Mid-Atlantic Ridge. Microorganisms that use H<sub>2</sub> and CH<sub>4</sub> as chemical energy are known to create diverse biological communities in the LCHF<sup>8,9</sup>, and thus it has been considered as an analogue environment to a place where life first appeared on our planet. Given that rocks constituting the LCHF are rich in olivine and have low Si content, a wide exposure of pyroxenite may have created a similar environment to the LCHF at most of the seafloor in the

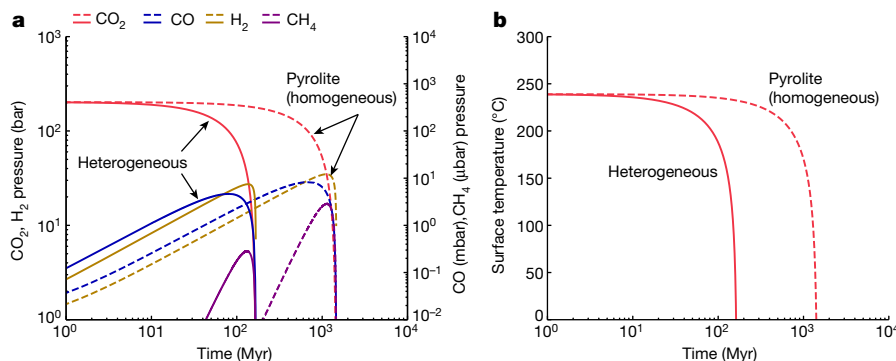


**Fig. 4 | Evolutions of atmospheric composition and surface temperature after the onset of plate tectonics.** **a**, Atmospheric evolution is shown for the cases of chemically heterogeneous (solid) and homogeneous (pyrolitic) mantles (dashed). Colour indicates gaseous species: CO<sub>2</sub> (red), CO (blue), H<sub>2</sub> (yellow), and CH<sub>4</sub> (purple).

The initial amount of CO<sub>2</sub> is set to 200 bar, which is the amount degassed from a magma ocean with 300 ppm of CO<sub>2</sub>, and the model calculations are performed until all CO<sub>2</sub> is sequestered to the mantle. **b**, Surface temperature evolution based on a 1D atmospheric model.

early Hadean. Alkaline conditions may also develop in an environment resembling hydrothermal vents, and, combined with the high dissolution rate of olivine, abiotic synthesis of ribose may have occurred<sup>50</sup>.

The aftermath of magma ocean solidification has a profound impact on characterizing the surface environment during the Hadean. Given that a habitable environment had emerged by 4.0 Ga, the Hadean evolution is explained more naturally by the mantle with a chemically heterogeneous structure. Small-scale heterogeneities would eventually be homogenized with high-Mg# pyroxenite as convective mixing proceeds, but homogenization is likely to take a few tens to hundreds of million of years to complete<sup>51</sup>. In the meantime, rapid plate motion would have continued. A faster plate motion accompanies a larger flux of upwelling mantle at mid-ocean ridges, so volatiles (including greenhouse gases) in the mantle would efficiently be released to the atmosphere. As sequestration removes CO<sub>2</sub> from the atmosphere, the intake and release of CO<sub>2</sub> would balance after some time, setting an initial condition for the Archean evolution. Also, residual CO<sub>2</sub> may have reacted with hydrogen produced by serpentinization to create a reduced atmosphere (Fig. 4). This may explain the potentially high abundance of CH<sub>4</sub> in the Archean atmosphere<sup>20</sup>. On the other hand, hydrous minerals are vulnerable to dehydration upon subduction, so a rapid plate motion would result in a net increase in surface water through degassing at ridges. Given a higher processing rate than the present-day mantle, the Hadean mantle would have dried out in approximately 500 Myr (see Methods), and an initially small ocean mass would have increased to the present-day level or higher by the beginning of the Archean. These are order-of-magnitude arguments but are consistent with the prominent features of the Archean Earth<sup>20,26,33</sup>. Our study provides a new perspective on the evolution of Hadean surface environment by bringing together the models of magma ocean solidification, atmospheric evolution and mantle convection.

## Online content

Any methods, additional references, Nature Research reporting summaries, source data, extended data, supplementary information, acknowledgements, peer review information; details of author contributions and competing interests; and statements of data and code availability are available at <https://doi.org/10.1038/s41586-021-04371-9>.

1. Matsui, T. & Abe, Y. Evolution of an impact-induced atmosphere and magma ocean on the accreting Earth. *Nature* **319**, 303–305 (1986).
2. Tonks, W. B. & Melosh, H. J. Magma ocean formation due to giant impacts. *J. Geophys. Res.* **98**, 5319–5333 (1993).
3. Canup, R. M. & Asphaug, E. Origin of the Moon in a giant impact near the end of the Earth's formation. *Nature* **412**, 708–712 (2001).
4. Wilde, S. A., Valley, J. W., Peck, W. H. & Graham, C. M. Evidence from detrital zircons for the existence of continental crust and oceans on the Earth 4.4 Gyr ago. *Nature* **409**, 175–178 (2001).
5. Harrison, T. M. The Hadean crust: Evidence from >4 Ga zircons. *Annu. Rev. Earth Planet. Sci.* **37**, 479–505 (2009).
6. Sleep, N. H. & Zahnle, K. Carbon dioxide cycling and implications for climate on ancient Earth. *J. Geophys. Res.* **106**, 1373–1399 (2001).
7. Kelley, D. S. et al. A serpentinite-hosted ecosystem: the Lost City Hydrothermal Field. *Science* **307**, 1428–1434 (2005).
8. Proskurowski, G. et al. Abiogenic hydrocarbon production at Lost City hydrothermal field. *Science* **319**, 604–607 (2008).
9. Klein, F., Grozeva, N. G. & Seewald, J. S. Abiotic methane synthesis and serpentinization in olivine-hosted fluid inclusions. *Proc. Natl Acad. Sci.* **116**, 17666–17672 (2019).
10. Raymond, S. N., Schlichting, H. E., Hersant, F. & Selsis, F. Dynamical and collisional constraints on a stochastic late veneer on the terrestrial planets. *Icarus* **226**, 671–681 (2013).
11. Krissansen-Totton, J., Arney, G. N. & Catling, D. C. Constraining the climate and ocean pH of the early Earth with a geological carbon cycle model. *Proc. Natl Acad. Sci.* **115**, 4105–4110 (2018).
12. Elkins-Tanton, L. T. Linked magma ocean solidification and atmospheric growth for Earth and Mars. *Earth Planet. Sci. Lett.* **271**, 181–191 (2008).
13. Lebrun, T. et al. Thermal evolution of an early magma ocean in interaction with the atmosphere. *J. Geophys. Res. Planet.* **118**, 1155–1176 (2013).
14. Hamano, K., Abe, Y. & Genda, H. Emergence of two types of terrestrial planet on solidification of magma ocean. *Nature* **497**, 607–610 (2013).

15. Salvador, A. et al. The relative influence of H<sub>2</sub>O and CO<sub>2</sub> on the primitive surface conditions and evolution of rocky planets. *J. Geophys. Res. Planet.* **122**, 1458–1486 (2017).
16. Bower, D. J. et al. Linking the evolution of terrestrial interiors and an early outgassed atmosphere to astrophysical observations. *Astron. Astrophys.* **631**, A103 (2019).
17. Hirschmann, M. M. Magma ocean influence on early atmosphere mass and composition. *Earth Planet. Sci. Lett.* **341–344**, 48–57 (2012).
18. Deng, J., Du, Z., Karki, B. B., Ghosh, D. B. & Lee, K. K. A magma ocean origin to divergent redox evolutions of rocky planetary bodies and early atmospheres. *Nat. Commun.* **11**, 2007 (2020).
19. Abe, Y. Physical state of the very early Earth. *Lithos* **30**, 223–235 (1993).
20. Catling, D. C. & Zahnle, K. J. The Archean atmosphere. *Sci. Adv.* **6**, eaax1420 (2020).
21. Solomatov, V. S. In *Treatise on Geophysics*. Volume 9: Evolution of the Earth 1st edn (ed. Schubert G.) 91–119 (Elsevier, 2007).
22. Hier-Majumder, S. & Hirschmann, M. M. The origin of volatiles in the Earth's mantle. *Geochem. Geophys. Geosyst.* **18**, 3078–3092 (2017).
23. Kawamoto, T. & Holloway, J. R. Melting temperature and partial melt chemistry to H<sub>2</sub>O-saturated mantle peridotite to 11 gigapascals. *Science* **276**, 240–243 (1997).
24. Katz, R. F., Spiegelman, M. & Langmuir, C. H. A new parameterization of hydrous mantle melting. *Geochem. Geophys. Geosyst.* **4**, 1073 (2003).
25. Hirschmann, M. M. & Dasgupta, R. The H/C ratios of Earth's near-surface and deep reservoirs, and consequences for deep Earth volatile cycles. *Chem. Geol.* **262**, 4–16 (2009).
26. Korenaga, J., Planavsky, N. J. & Evans, D. A. D. Global water cycle and the coevolution of the Earth's interior and surface environment. *Philos. Trans. R. Soc. A* **375**, 20150393 (2017).
27. Maurice, M. et al. Onset of solid-state mantle convection and mixing during magma ocean solidification. *J. Geophys. Res. Planet.* **122**, 577–598 (2017).
28. Miyazaki, Y. & Korenaga, J. On the timescale of magma ocean solidification and its chemical consequences: 2. Compositional differentiation under crystal accumulation and matrix compaction. *J. Geophys. Res. Solid Earth* **124**, 3399–3419 (2019).
29. Blank, J. G. & Brooker, R. A. In *Reviews in Mineralogy and Geochemistry*. Volume 30: Volatiles in Magmas (eds Carrol, M. R. & Holloway, J. R.) 157–186 (Mineralogical Society of America, 1994).
30. Abe, Y. In *Evolution of the Earth and Planets* (eds Takahashi, E. et al.) 41–54 (AGU, 1993).
31. Hirth, G. & Kohlstedt, D. L. Water in the oceanic upper mantle: implications for rheology, melt extraction and the evolution of the lithosphere. *Earth Planet. Sci. Lett.* **144**, 93–108 (1996).
32. Jain, C., Korenaga, J. & Karato, S.-i. Global analysis of experimental data on the rheology of olivine aggregates. *J. Geophys. Res. Solid Earth* **124**, 310–334 (2019).
33. Korenaga, J. Thermal evolution with a hydrating mantle and the initiation of plate tectonics in the early Earth. *J. Geophys. Res.* **116**, B12403 (2011).
34. Korenaga, J. Plate tectonics and surface environment: role of the oceanic upper mantle. *Earth Sci. Rev.* **205**, 103185 (2020).
35. Zahnle, K. et al. Emergence of a habitable planet. *Space Sci. Rev.* **129**, 35–78 (2007).
36. Korenaga, J. Energetics of mantle convection and the fate of fossil heat. *Geophys. Res. Lett.* **30**, 1437 (2003).
37. Bradley, D. C. Passive margins through earth history. *Earth Sci. Rev.* **91**, 1–26 (2008).
38. Herzberg, C., Condie, K. & Korenaga, J. Thermal history of the Earth and its petrological expression. *Earth Planet. Sci. Lett.* **292**, 79–88 (2010).
39. Pehrsson, S. J., Eglinton, B. M., Evans, D. A., Huston, D. & Reddy, S. M. Metallogeny and its link to orogenic style during the Nuna supercontinent cycle. *Geol. Soc. Spec. Publ.* **424**, 83–94 (2016).
40. Plesa, A.-C., Tosi, N. & Breuer, D. Can a fractionally crystallized magma ocean explain the thermo-chemical evolution of Mars? *Earth Planet. Sci. Lett.* **403**, 225–235 (2014).
41. Ghiorso, M. S., Hirschmann, M. M., Reiners, P. W. & Kress, V. C. III The pMELTS: A revision of MELTS for improved calculation of phase relations and major element partitioning related to partial melting of the mantle to 3 GPa. *Geochem. Geophys. Geosyst.* **3**, 1–35 (2002).
42. Gualda, G. A., Ghiorso, M. S., Lemons, R. V. & Carley, T. L. Rhyolite-MELTS: a modified calibration of MELTS optimized for silica-rich, fluid-bearing magmatic systems. *J. Petrol.* **53**, 875–890 (2012).
43. Korenaga, J. In *Archean Geodynamics and Environments* (eds Benn, K. et al.) 7–32 (AGU, 2006).
44. Davies, G. F. On the emergence of plate tectonics. *Geology* **20**, 963–966 (1992).
45. Korenaga, J. Scaling of plate tectonic convection with pseudoplastic rheology. *J. Geophys. Res.* **115**, B11405 (2010).
46. Diamond, L. W. & Akinfiev, N. N. Solubility of CO<sub>2</sub> in water from –1.5 to 100 °C and from 0.1 to 100 MPa: evaluation of literature data and thermodynamic modelling. *Fluid Phase Equilib.* **208**, 265–290 (2003).
47. Alt, J. C. & Teagle, D. A. The uptake of carbon during alteration of ocean crust. *Geochim. Cosmochim. Acta* **63**, 1527–1535 (1999).
48. Sleep, N. H., Meibom, A., Fridriksson, T., Coleman, R. G. & Bird, D. K. H<sub>2</sub>-rich fluids from serpentinization: geochemical and biotic implications. *Proc. Natl Acad. Sci.* **101**, 12818–12823 (2004).
49. Schulte, M., Blake, D., Hoehler, T. & McCollom, T. Serpentinization and its implications for life on the early Earth and Mars. *Astrobiology* **6**, 364–376 (2006).
50. Lambert, J. B., Gurusamy-Thangavelu, S. A. & Ma, K. The silicate-mediated formose reaction: bottom-up synthesis of sugar silicates. *Science* **327**, 984–986 (2010).
51. Davies, G. F. Gravitational depletion of the early Earth's upper mantle and the viability of early plate tectonics. *Earth Planet. Sci. Lett.* **243**, 376–382 (2006).

**Publisher's note** Springer Nature remains neutral with regard to jurisdictional claims in published maps and institutional affiliations.

© The Author(s), under exclusive licence to Springer Nature Limited 2022

## Methods

### Degassing of magma ocean

#### Volatile partitioning between magma ocean and atmosphere.

We solve for the degassing of the mantle based on volatile partitioning between the atmosphere and the mantle. The atmosphere and the melt phase at the surface of a magma ocean are assumed to be in equilibrium, so for each volatile component  $i$ , the concentration in the surface magma,  $x_i$ , is calculated from the solubility at its partial pressure,  $P_i$ . When the mass of the melt-dominated layer is  $M_l$ , the following mass balance holds<sup>16</sup>

$$x_i \phi M_l + \frac{\mu_i}{\bar{\mu}} \frac{4\pi R_e^2}{g} P_i = m_i, \quad (1)$$

where  $\phi$  is the melt fraction at the surface of a magma ocean,  $\mu_i$  is the molar mass of either H<sub>2</sub>O or CO<sub>2</sub>,  $\bar{\mu}$  is the mean molar mass of the atmosphere,  $R_e$  is the Earth's radius,  $g$  is gravity, and  $m_i$  is the total mass of the volatile under consideration in the melt-dominated layer and the atmosphere (see Fig. 1a). The first term indicates the volatile budget in the melt-dominated layer, where  $x_i \phi$  is the bulk volatile concentration in a crystal-melt mixture of the melt-dominated layer. As a result of rapid convection, this bulk volatile concentration is assumed to be constant throughout the melt-dominated layer. For solubility, we adopt the parameterization of Blank and Brooker<sup>29</sup>, and

$$P_{\text{H}_2\text{O}}(x_{\text{H}_2\text{O}}) = \left( \frac{x_{\text{H}_2\text{O}}}{6.8 \times 10^{-8}} \right)^{1.42}, \quad (2)$$

and

$$P_{\text{CO}_2}(x_{\text{CO}_2}) = \left( \frac{x_{\text{CO}_2}}{4.4 \times 10^{-12}} \right), \quad (3)$$

are used for water and CO<sub>2</sub>, respectively. Note that  $x_{\text{H}_2\text{O}}$  and  $x_{\text{CO}_2}$  are given in terms of mass fraction. Melt fraction at the surface  $\phi$  is calculated from the surface temperature, which is estimated using a 1D atmospheric model. The surface temperature,  $T_s$ , is a function of the atmospheric mass and composition and the net outgoing infrared radiation, and the outgoing radiation,  $F_{\text{out}}$ , is described as the sum of absorbed sunlight and convective heat flux<sup>21,52</sup>:

$$F_{\text{out}} = (1 - A)F_{\odot} + 0.089 \frac{k_T(T_m - T_s)}{d} \text{Ra}^{1/3}, \quad (4)$$

where  $A$  is the albedo,  $F_{\odot}$  is solar flux (values discussed later in Methods section 'Atmospheric model'),  $k_T$  is thermal conductivity ( $4 \text{ W m}^{-1} \text{ K}^{-1}$ ),  $T_m$  is mantle potential temperature,  $d$  is the depth of the melt-dominated layer, and  $\text{Ra}$  is the Rayleigh number of the melt-dominated layer. This value is set as  $F_{\uparrow}$  at  $\tau = 0$  in the atmospheric model.

At the beginning of the evolution, the entire mantle is assumed to be melt-dominated, and  $M_l$  is set to the mass of the entire mantle. The initial mass of volatile  $m_i$  is calculated from the initial volatiles concentration, which is assumed to be 0.04–0.1 wt% for water and 200–500 ppm for CO<sub>2</sub>. As a magma ocean solidifies and the melt-dominated layer shrinks, the solid-dominated layer grows from the bottom of the mantle. Volatiles would be trapped in the porous melt phase of the solid-dominated layer, so when  $\Delta M$  of the mantle solidifies to be solid-dominated and the melt-dominated layer shrinks by  $\Delta d$ ,  $\Delta M x_i \phi$  of volatiles would be removed from the volatile budget of the melt-dominated layer  $m_i$ :

$$m_i(d - \Delta d) = m_i(d) - \Delta M x_i \phi. \quad (5)$$

Equations (1)–(5) are solved as the melt-dominated layer solidifies until  $d = 0$ . The evolution of volatile budget is summarized in Extended Data Table 1.

**Degassing of a magma ocean during the last phase of its solidification.** When the melt-dominated layer disappears, the upper part of the mantle, although rheologically solid, remains partially molten. When upward melt percolation is faster than solid-state convection, volatiles contained in the partially molten layer are expected to be released to the atmosphere (Fig. 1b). As partial melt approaches the surface and solidifies, volatiles concentrate in the residual melt phase. Volatiles eventually exceed the saturation limit, and thus volatiles in the near-surface region would have degassed efficiently. We compare the timescales of melt percolation,  $t_{\text{perc}}$ , and convection,  $t_{\text{conv}}$ , to determine the depth where melt and volatiles can be extracted to the surface.

The timescale of melt percolation from a depth of  $D$  to the surface is given by

$$t_{\text{perc}} = \frac{D}{v_{\text{perc}}}, \quad (6)$$

where  $v_{\text{perc}}$  is percolation velocity<sup>53</sup>,

$$v_{\text{perc}} = \frac{d^2 g \Delta \rho}{150 \eta_l (1 - \phi)}. \quad (7)$$

Here  $d$  denotes the grain size of solid matrix,  $g$  is gravity,  $\Delta \rho$  is the density difference between the melt and solid phases,  $\eta_l$  is the melt viscosity and  $\phi$  is melt fraction. For  $d = 1 \text{ mm}$ ,  $g = 9.8 \text{ m s}^{-2}$ ,  $\Delta \rho = 400 \text{ kg m}^{-3}$ , and  $\eta_l = 1 \text{ Pa s}$ ,

$$t_{\text{perc}} \approx 2.5 \left( \frac{D}{200 \text{ km}} \right) \left( \frac{0.01}{\phi} \right)^2 \text{ Myr}. \quad (8)$$

The convective timescale is scaled using plate velocity as

$$t_{\text{conv}} = \frac{D}{v_s} \approx 4.0 \left( \frac{D}{200 \text{ km}} \right) \left( \frac{v_s}{5.0 \text{ cm yr}^{-1}} \right) \text{ Myr}, \quad (9)$$

where  $v_s$  is plate velocity, whose formulation is described in a later section. These suggest that a partially molten layer with  $\phi > 0.01$  is expected to become depleted in porous melt and thus volatiles.

The thickness of the partially molten layer is estimated from an adiabat with a melt fraction of 0.4 at the surface because the rapid Rayleigh–Taylor instability<sup>27,28</sup> should have maintained an adiabatic temperature profile within the solid-dominated layer. A melt fraction of 0.4 marks the rheological transition of a partially molten medium<sup>21,30</sup>, and the Rhyolite–MELTS model<sup>42</sup> is used to estimate melt fraction. For the chemically heterogeneous mantle with 0.1 wt% water, the melt-dominated layer would disappear at a potential temperature of  $-1,625 \text{ }^\circ\text{C}$ , and the high-Mg# pyroxenite would be partially molten up to a depth of  $-4 \text{ GPa}$  (Extended Data Fig. 1). The chemically heterogeneous mantle consists of a mixture of iron-rich blobs and a high-Mg# pyroxenite matrix, so its average melt fraction should be 0.4 when the mantle starts to behave rheologically as solid. The magma ocean model of ref. <sup>28</sup>, suggests that the mass fraction of iron-rich blobs is about a quarter of the entire mantle, but because they are of small scale and not interconnected, the partial melt of iron-rich blobs is not considered to escape by percolation. We thus assume that volatiles contained in the top  $-4 \text{ GPa}$  would be released to the atmosphere in Fig. 2. It is noted that the melt-dominated layer would disappear at a potential temperature of  $-1,600 \text{ }^\circ\text{C}$  for a pyrolitic mantle (Extended Data Fig. 2). Therefore, the entire mantle is assumed to be rheologically solid at a potential temperature of  $1,600 \text{ }^\circ\text{C}$  for both chemically homogeneous and heterogeneous mantles, and these thermal structures are adopted as initial conditions for subsequent calculations.

We note that a small amount of degassing by episodic eruptions may also take place during the transition from magma ocean to solid-state

convection. Our model assumes that the Rayleigh–Taylor instability efficiently cools the solid-dominated layer<sup>27,28</sup>, and the layer maintains an adiabatic thermal profile within the timescale of magma ocean solidification. Cooling, however, could be inhibited by tidal heating<sup>54</sup>, and such heat may be released by episodic eruptions in addition to convective heat flux after the solidification of the mantle surface. Consequently, water degassing could be promoted, and ocean mass may increase rapidly. Yet, the interplay between tidal heating, cooling by the Rayleigh–Taylor instability, and melt percolation remains unconstrained, and future work is required to quantify the degree of degassing during this period. Episodic eruptions, however, would not affect the overall mode of mantle dynamics. Erupted melt would be recycled to the mantle by plate tectonics, and the rate of carbon sequestration is expected to remain unchanged from our model results.

## The composition of the chemically heterogeneous mantle

The fractional crystallization of a magma ocean produces a structure dominated by the high-Mg# matrix with small iron-rich blobs (Fig. 3a, Extended Data Fig. 1d). Ref. <sup>28</sup> estimated that the ternary composition of the high-Mg# matrix is on average MgO 41.7 wt%, FeO 4.4 wt% and SiO<sub>2</sub> 53.9 wt%, whereas that of iron-rich blobs is MgO 41.0 wt%, FeO 20.6 wt% and SiO<sub>2</sub> 38.3 wt%. The Mg# of the two components are -94 and -77, respectively, resulting in a difference in density and melting temperature. It is noted that iron-rich blobs make up ~25% of the heterogeneous mantle, and the average composition of the mantle is consistent with the pyrolytic mantle.

The solidus of such a high-Mg# matrix is expected to be higher than that of a pyrolytic mantle, and we estimate the solidus temperature using the Rhyolite-MELTS model<sup>42</sup>. To predict the mineralogy of high-Mg# matrix, the Al<sub>2</sub>O<sub>3</sub> and CaO contents are estimated using a partitioning model described in the following paragraph. Combining the results of the partitioning model with the ternary composition, we obtain an estimate of MgO 39.5 wt%, FeO 4.1 wt%, SiO<sub>2</sub> 51.3 wt%, Al<sub>2</sub>O<sub>3</sub> 3.5 wt% and CaO 1.5 wt% for the high-Mg# matrix, which results in a mineral assemblage of 70 wt% pyroxene, 25 wt% olivine, 5 wt% spinel at 1,500 °C and 1.2 GPa. For Fe-rich blobs, a composition of MgO 37.8 wt%, FeO 19.0 wt%, SiO<sub>2</sub> 35.3 wt%, Al<sub>2</sub>O<sub>3</sub> 3.7 wt% and CaO 4.1 wt% is predicted, resulting in a mineral assemblage of 84 wt% olivine, 8 wt% of merwinite, 6 wt% of spinel and 2 wt% of periclase. The melt fraction of the two components is shown in Extended Data Fig. 1.

To predict the concentrations of Al<sub>2</sub>O<sub>3</sub> and CaO, we construct an element-partitioning model within the magma ocean, assuming that all newly formed crystals in the melt-dominated layer would stack at the base of the layer to form a rheologically rigid layer (Fig. 1a). This is the same as crystal accumulation in the model of ref. <sup>28</sup>. In a terrestrial magma ocean, crystals forming below the liquidus are predominantly bridgmanite under lower-mantle pressures, so at each time step, we calculate the amount of newly formed bridgmanite and estimate the partitioning of Al<sub>2</sub>O<sub>3</sub> and CaO between melt and bridgmanite. Bridgmanite would be incorporated in the growing rheologically rigid layer, which includes some amount of melt because the compaction of crystal-melt mixture can take place only slowly. The partitioning coefficients between melt and bridgmanite are estimated from the experimental results of refs. <sup>55,56</sup>, and we adopt values of  $D_{Al/Si} = 0.78$  and  $D_{Ca/Si} = 0.16$ .

The mantle is initially assumed to be entirely molten, and we run the model while newly formed bridgmanite is heavier than the remaining melt. The model of ref. <sup>28</sup> suggests that when the depth of the melt-dominated layer reaches 500 km, bridgmanite becomes lighter than the remaining melt and compositional fractionation ceases. The partitioning model indicates that the lower mantle, which eventually evolves into the high-Mg# matrix, would be depleted in CaO but shows little change in the Al<sub>2</sub>O<sub>3</sub> content from the initial after the solidification (Extended Data Fig. 4). We thus estimate that the high-Mg#

matrix would have concentrations of Al<sub>2</sub>O<sub>3</sub>  $3.6 \pm 0.7$  wt% and CaO  $1.51 \pm 0.11$  wt%.

## Atmospheric evolution after the solidification of the mantle surface

In our model, the removal of CO<sub>2</sub> from the atmosphere is governed by the formation of carbonates at ocean basins, which are sequestered to the mantle by subduction. At each time step, we remove CO<sub>2</sub> by carbonation formation, release H<sub>2</sub> by serpentinization, and update the surface temperature based on the new atmospheric pressure and composition. This procedure is repeated until all CO<sub>2</sub> in the atmosphere is sequestered to the mantle.

The timescale of CO<sub>2</sub> removal is assumed to be the same as that of ocean basins renewal, so the removal rate is proportional to the surface renewal rate and is inversely proportional to plate velocity. With the current plate construction rate<sup>57</sup> of 3.4 km<sup>2</sup> yr<sup>-1</sup>, which corresponds to the average plate velocity of 5 cm yr<sup>-1</sup>, the entire ocean basin is renewed every 90 Myr. The amount of carbonate formed at the seafloor is estimated based on the assumption that Ca and Mg silicates in the top 500 m of oceanic crust reacted with CO<sub>2</sub><sup>35</sup>, and we estimate that the Hadean seafloor contained ~14 bar of CO<sub>2</sub>, whereas current basaltic crust holds ~2.5 bar of atmospheric CO<sub>2</sub>. Details are discussed in a later section.

**Plate velocity.** When plate tectonics is operating, plate velocity,  $v_s$ , can be estimated from mantle heat flux,  $Q$ , as

$$v_s = v_{s,0} \left( \frac{Q \Delta T_0}{Q_0 \Delta T} \right)^2, \quad (10)$$

where  $\Delta T$  is the temperature difference between the surface and mantle. The subscript 0 indicates the present-day values;  $v_{s,0}$  is 5 cm yr<sup>-1</sup>,  $Q_0$  is 38 TW and  $\Delta T_0$  is 1,350 K. Mantle heat flux  $Q$  is calculated on the basis of the scaling of ref. <sup>45</sup>, which includes the effect of dehydration stiffening of depleted lithospheric mantle. Convective heat flux  $Q$  is given by

$$Q = \text{Nu} \frac{k_r A \Delta T}{L}, \quad (11)$$

where Nu is the Nusselt number,  $A$  is the surface area of Earth, and  $L$  is the mantle depth. The Nusselt number Nu is calculated as<sup>45</sup>

$$\text{Nu} = 2 \left( \frac{\text{Ra}_i}{\text{Ra}_c} \right)^{1/3} \Delta \eta_L^{-1/3}, \quad (12)$$

where  $\text{Ra}_i$  is the internal Rayleigh number,  $\text{Ra}_c$  is the critical Rayleigh number ( $\approx 1,000$ ), and  $\Delta \eta_L$  is the lithospheric viscosity contrast. The internal Rayleigh number is defined as

$$\text{Ra}_i = \frac{\alpha \rho g \Delta T L^3}{\kappa \eta}, \quad (13)$$

where  $\alpha$  is thermal expansivity,  $\rho$  is mantle density and  $\kappa$  is thermal diffusivity. Mantle viscosity,  $\eta$ , changes with temperature with an activation energy,  $E$ , of 300 kJ mol<sup>-1</sup>, and the reference viscosity is set to 10<sup>19</sup> Pa s at 1,350 °C. The lithospheric viscosity contrast  $\Delta \eta_L$  changes with the thickness of depleted lithospheric mantle,  $h_m$ , as:

$$\Delta \eta_L = \Delta \eta_{L,\text{ref}} \exp \left[ \ln(\Delta \eta) \min \left( 1, \frac{h_m}{6h_{\text{ref}}} \right) \right], \quad (14)$$

where  $\Delta \eta_{L,\text{ref}}$  is the reference viscosity contrast,  $\Delta \eta$  is the viscosity contrast induced by mantle dehydration, and  $h_{\text{ref}}$  is the thickness of thermal boundary layer in the absence of dehydration stiffening,  $L/\text{Nu}_{\text{ref}}$ . The reference viscosity contrast  $\Delta \eta_{L,\text{ref}}$  is parameterized as<sup>45</sup>

$$\Delta\eta_{L,ref} = \exp\left(0.326\left(\frac{\mu}{\alpha\Delta T}\right)^{0.647}\theta\right), \quad (15)$$

where  $\mu$  is an effective friction coefficient and  $\theta$  is a nondimensionalized activation energy (known as the Frank–Kamenetskii parameter),

$$\theta = \frac{E\Delta T}{RT_p^2}, \quad (16)$$

where  $R$  is the universal gas constant and  $T_p$  is mantle potential temperature. To reproduce the present-day heat flux of 38 TW, we adopt  $\Delta\eta = 100$  and  $\mu = 0.025$ . These values indicate that a dry mantle has a viscosity 100 times greater than the present-day convecting mantle, and a mantle with a potential temperature of 1,600 °C is 20 times less viscous than that of 1,350 °C with the same degree of dehydration. It is noted that the rheology of the chemically heterogeneous mantle is expected to be similar to that of a pyrolytic mantle. The pyroxenite matrix contains 25% of olivine, which is a threshold for a phase to be interconnected, and thus its rheology would also be governed by olivine. Even if olivine grains are not interconnected, enstatite aggregates are expected to have similar viscosity to olivine aggregates under dislocation creep at temperatures expected for the Hadean mantle<sup>58</sup>.

The difference in plate velocity between the chemically homogeneous and heterogeneous mantles arises from  $h_m$ . Because a hotter mantle with the same composition would melt by a larger degree, the value of  $h_m$  for a pyrolytic mantle would be greater than that for the (colder) present-day mantle. To predict the thickness of dehydrated lithosphere, a fractional melting model is constructed on the basis of the melting model of ref.<sup>24</sup>. Assuming that a fraction of the partial melt escapes to the surface with each increment of new melting (see the legends of Extended Data Figs. 1, 2), the depleted lithospheric mantle would thicken to -140 km (4.5 GPa) for a mantle potential temperature of 1,600 °C, from -60 km (2 GPa), which is the thickness for the present-day depleted lithospheric mantle (Extended Data Fig. 2). On the other hand, the value of  $h_m$  for the chemically heterogeneous mantle is predicted to be -40 km based on the Rhyolite-MELTS model<sup>42</sup>, and the initial depth of melting has been corroborated with the pMELTS model<sup>41</sup>. Because the high-Mg# pyroxenite starts to melt at a shallower depth than a pyrolytic homogeneous mantle, and also because the partition coefficient of water between pyroxene and melt is larger than that between olivine and melt, we estimate that the mantle would not be completely dehydrated until 2 GPa. A value of 0.02 is adopted for water partitioning between the pyroxenite matrix and melt, and 0.005 for partitioning between pyrolite and melt<sup>59</sup>. It is noted that iron-rich blobs would melt at a depth deeper than 10 GPa (Extended Data Fig. 1c), but the melting of blobs only creates locally depleted regions and thus is unlikely to affect the overall value of  $h_m$ .

A buoyancy constraint would further limit the plate velocity for a pyrolytic mantle<sup>43,44</sup> (Fig. 3c). The thicknesses of buoyant basaltic crust and depleted lithospheric mantle increase as the mantle becomes hotter, and thus the thermal boundary layer needs to grow sufficiently thick for plate to be negatively buoyant. The densities of oceanic crust and depleted lithospheric mantle are estimated using a model of ref.<sup>43</sup>, and to become negatively buoyant, the subduction age of plate is set to the critical age of lithosphere. Such a buoyancy constraint, however, does not apply for the case of chemically heterogeneous mantle. The melting of high-Mg# pyroxenite matrix would also produce buoyant oceanic crust at the surface, but its thickness is -4 km, 15% of crust formed from a pyrolytic mantle (Fig. 3b). Also, crust created by the melting of iron-rich blobs would act as a weight within a crust to promote subduction because iron-rich crust would have an Mg# of 56 and a density over 3,500 kg m<sup>-3</sup> (Extended Data Table 2). Fe-rich

blobs start to melt at a deeper depth, so the crust produced by the melting of blobs would have an average thickness of -11 km. The crust of the chemically heterogeneous mantle would not be uniform, but the average crustal thickness is predicted to be -15 km, -70% of which originates from Fe-rich blobs. It is noted that the density of partial melt from iron-rich blobs is estimated to be 3,000 kg m<sup>-3</sup>, which is still lower than the high-Mg# matrix. Partial melt from iron-rich blobs would thus migrate upwards within the high-Mg# matrix. The density difference between iron-rich melt and the matrix is approximately four times smaller than that between partial melt from the matrix and the matrix itself, so these two kinds of partial melt may migrate upward without much mixing. The large fraction of the iron-rich crust may be situated below the high-Mg# crust, but some amount of iron-rich crust would be exposed at the surface, promoting H<sub>2</sub> and CH<sub>4</sub> production at the seafloor. Crustal composition is calculated by averaging the compositions of partial melt from the high-Mg# pyroxenite, and its mineral assemblage is estimated at 250 °C and 10 bar using Theriak-Domino<sup>60</sup> (Extended Data Table 2).

The thicknesses of crust and depleted lithospheric mantle are estimated on the basis of an adiabatic temperature profile of the upper mantle. Adiabatic gradient is calculated using<sup>61</sup>

$$\left(\frac{dT}{dP}\right)_s = \phi \frac{\alpha_l T}{\rho_l c_p} + (1 - \phi) \frac{\alpha_s T}{\rho_s c_p} - \frac{T\Delta S}{c_p} \left(\frac{d\phi}{dP}\right)_s, \quad (17)$$

where  $\phi$  is melt fraction,  $\alpha$  is thermal expansivity,  $\rho$  is density,  $c_p$  is specific heat per unit mass, and  $\Delta S$  is entropy change upon melting. Subscripts l and s denote the melt and liquid phases, respectively. Values adopted for thermal expansivity are 3.0 and  $4.6 \times 10^{-5} \text{ K}^{-1}$  for  $\alpha_s$  and  $\alpha_l$ , and, for density,  $\rho_l$  and  $\rho_s$  are taken to be 2,900 and 3,300 kg m<sup>-3</sup>, respectively. We adopt 1,000 J kg<sup>-1</sup> K<sup>-1</sup> for  $c_p$  and 300 J kg<sup>-1</sup> K<sup>-1</sup> for  $\Delta S$ . The term  $d\phi/dP$  in equation (17) is determined so that changes in  $T$  and  $\phi$  are consistent with both equation (17) and the melting model. The effect of hydration on melting temperature depression is adopted from ref.<sup>24</sup> as

$$\Delta T(x_{\text{H}_2\text{O}}) = 0.43 \times x_{\text{H}_2\text{O}}^{0.75} \text{ K}, \quad (18)$$

where  $x_{\text{H}_2\text{O}}$  is the weight % of dissolved water content in the melt. Melting temperature decreases by a larger degree as melt fraction approaches zero, and the degree of decrease is largest at the solidus.

The evolution of mantle potential temperature  $T_p$  is solved using the following global heat balance equation<sup>62</sup>:

$$C \frac{dT_p}{dt} = H - Q, \quad (19)$$

where  $C$  is the heat capacity of Earth ( $7 \times 10^{27} \text{ J K}^{-1}$ ) and  $H$  is internal heat production by <sup>238</sup>U, <sup>235</sup>U, <sup>232</sup>Th and <sup>40</sup>K. Internal heat production is calculated using a parameterization by ref.<sup>43</sup>. We assume an initial potential temperature of 1,600 °C for both chemically homogeneous and heterogeneous mantles, as explained previously.

**Mantle degassing by plate tectonics.** Given that the current rate of plate construction<sup>57</sup> is 3.4 km<sup>2</sup> yr<sup>-1</sup> and that the initial depth of mantle melting is -60 km, the processing rate of the present-day mantle is estimated to be  $-6.7 \times 10^{14} \text{ kg yr}^{-1}$ , suggesting that it takes -6 Gyr to process the entire mantle. For the chemically heterogeneous mantle, plate velocity is faster by -9 times than the present, and the top 2–3 GPa would be dehydrated during the mantle upwelling (see Extended Data Fig. 1). Therefore, the processing timescale of the chemically heterogeneous mantle is predicted to be shortened by a factor of 10–15 or to -400–600 Myr, suggesting that the entire mantle was mostly processed by the end of Hadean. Therefore, the mantle would have become mostly dry by then, and majority of the water budget would reside at the surface.

**The operation of plate tectonics.** For plate tectonics to operate, the negative buoyancy of the cold lithosphere should be large enough to bend subducting plates. It is noted that the term plate tectonics here refers to a mode of mantle convection that allows for the recycling of the surface layer, and plate kinematics could be different from modern-style plate tectonics. The criterion for plate tectonics is parameterized as<sup>45</sup>

$$\Delta\eta_L \leq 0.25Ra_1^{1/2} \equiv \Delta\eta_{L,crit}, \quad (20)$$

where  $\Delta\eta_{L,crit}$  denotes the critical value for the operation of plate tectonics. For both chemically homogeneous and heterogeneous mantles, the lithospheric viscosity contrast is smaller than the critical value (Extended Data Fig. 5), and thus plate tectonics is possible in the Hadean. Because water oceans were probably present at the surface, we consider that thermal cracking weakened the stiff lithosphere<sup>63</sup> to reduce the value of effective friction coefficient to  $\mu = 0.02$ – $0.03$ . The existence of oceans is the key to plate tectonics, because, if water oceans were absent in the Hadean, the value of  $\mu$  increases to  $\sim 0.8$ , resulting in a large lithospheric viscosity contrast. In such a case, the Hadean Earth would have operated under the stagnant lid mode, which lacks the recycling of the surface.

**The fate of iron-rich blobs.** With a mantle potential temperature of  $1,600^\circ\text{C}$ , the high-Mg# pyroxenite matrix would experience  $\sim 27\%$  melting, whereas iron-rich blobs would melt up to  $\sim 43\%$  when blobs maintain a thermal equilibrium with the pyroxenite matrix (Extended Data Fig. 1c). Iron-rich blobs are predominantly consisted of olivine, and the partial melt would be further enriched in iron. The Rhyolite-MELTS model<sup>42</sup> predicts that such a crust has a composition of MgO 16.0 wt%, FeO 22.9 wt%, SiO<sub>2</sub> 39.2 wt%, Al<sub>2</sub>O<sub>3</sub> 9.2 wt%, and CaO 12.6 wt%, resulting in an Mg# of 56 and a crustal density higher than  $3,500\text{ kg m}^{-3}$  (Extended Data Table 2). The melt density of partial melt from iron-rich blobs is  $3,000\text{ kg m}^{-3}$ , which is still lower than the density of the pyroxenite matrix, so the iron-rich melt would migrate upward.

The preexisting lithological heterogeneities (high-Mg# matrix and iron-rich blobs) as well as the newly generated heterogeneities (crustal products and solid residues) would eventually be homogenized as the mantle evolves, but timescale for mixing depends on many uncertain parameters<sup>64</sup>. For example, the subducted iron-rich crust would be denser than ambient mantle, so it may stay longer in the lower mantle without being homogenized with the entire mantle<sup>51</sup>. It is not unrealistic to expect that the initial heterogeneity survived until the end of the Hadean.

**Atmospheric model.** The surface temperature is calculated using a 1D radiative–convective atmosphere model of ref. <sup>65</sup>. This model assumes that the atmosphere is grey to outgoing infrared radiation but transparent to incoming solar visible radiation. The atmosphere consists of two layers, stratosphere and troposphere, where temperature in the stratosphere is controlled by radiative equilibrium, whereas convective heat transport from the bottom governs the thermal structure in the troposphere. The atmosphere is assumed to be plane-parallel and is transparent to solar radiation, but opaque to infrared radiation regardless of the wavelength. For simplicity, the effects of clouds are neglected in our model.

We assume that the early Earth atmosphere contains 1 bar of N<sub>2</sub> with a varying mixture of CO<sub>2</sub> and H<sub>2</sub>O, which are determined based on the partitioning of volatiles between a magma ocean and the atmosphere. Sulfur and chloride volatiles may have also contributed to the greenhouse effect<sup>66</sup>, but its effect is likely to be smaller compared to that created by a thick atmosphere of CO<sub>2</sub> and H<sub>2</sub>O. A solar constant 30% smaller than the present is adopted to account for the faint young Sun, and the planetary albedo is fixed at 0.3. The hydrodynamic escape

of volatiles is not included in this model for simplicity, although its effect would be significant for the case of homogeneous mantle, the evolutionary timescale of which exceeds 1 Gyr.

The temperature structure in the stratosphere is calculated using radiative equilibrium, which can be written as a function of optical thickness,  $\tau$ :

$$\sigma_B T(\tau)^4 = \frac{1}{2} F_{\text{net}} \left( \frac{3}{2} \tau + 1 \right), \quad (21)$$

where  $\sigma_B$  is the Stefan–Boltzmann constant and  $F_{\text{net}}$  is the net infrared flux emitted from the top of the atmosphere. Upwards,  $F_{\uparrow}$ , and downwards,  $F_{\downarrow}$ , radiation fluxes are also calculated as

$$F_{\uparrow}(\tau) = \frac{1}{2} F_{\text{net}} \left( \frac{3}{2} \tau + 2 \right), \quad (22)$$

$$F_{\downarrow}(\tau) = \frac{1}{2} F_{\text{net}} \left( \frac{3}{2} \tau \right). \quad (23)$$

Optical thickness  $\tau$  is defined so that it increases towards the Earth's surface:

$$\tau(z) = - \int_{\infty}^z \kappa \rho_g dz, \quad (24)$$

where  $\kappa$  denotes the Rosseland mean opacity. Opacity  $\kappa$  depends on the atmospheric concentrations of greenhouse gases, and for the atmosphere, which has a molar fraction of  $x_i$  of gas species  $i$ ,  $\kappa$  is given by

$$\kappa = \frac{1}{\bar{\mu}} \sum_i \kappa_i x_i \mu_i, \quad (25)$$

where  $\bar{\mu}$  is the mean molar mass of gas, and  $\kappa_i$  and  $\mu_i$  are the opacity and molar mass, respectively, of species  $i$ . For opacity, we use  $10^{-2}$  for H<sub>2</sub>O,  $1.3 \times 10^{-4}$  for CO<sub>2</sub><sup>67</sup>, and 0 for N<sub>2</sub>, assuming N<sub>2</sub> is transparent to infrared radiation. The composition of the atmosphere is assumed to be uniform in the stratosphere.

In the troposphere, the thermal structure is controlled by the moist adiabatic lapse rate, which is given by

$$\left( \frac{dT}{dP} \right) = \frac{\bar{\mu}}{\rho_g c_p} \frac{1 + \frac{qL_w}{RT}}{1 + \frac{qL_w^2}{c_p RT^2}}, \quad (26)$$

where  $\rho_g$  is the mean gas density,  $q$  is water mixing ratio,  $L_w$  is the latent heat of the water, and  $R$  is the universal gas constant. Water mixing ratio  $q$  is set to be saturated, which is probable in a CO<sub>2</sub>-dominated atmosphere, and is obtained from the water phase diagram. The tropopause, a boundary between the stratosphere and troposphere, is determined as the height at which the radiation energy is balanced. The upward radiation flux emitted from the troposphere can be calculated as

$$F_{\uparrow}(\tau) = -\sigma_B T^4 + \int_{\tau_b}^{\tau} e^{-(\tau'-\tau)} \frac{d}{d\tau'} (\sigma_B T(\tau')^4) d\tau', \quad (27)$$

where  $\tau_b$  is the optical depth at the bottom of the atmosphere. We assume that the upward flux at the ground is the blackbody radiation of the ground temperature ( $F_{\uparrow, \text{surf}} = -\sigma_B T_{\text{surf}}^4$ ). At the optical depth of the tropopause,  $\tau_p$ , the values of  $F_{\uparrow}(\tau_p)$  calculated from equations (22) and (27) should be identical to satisfy the energy balance. We search for the profiles of temperature and water vapour content that agree with energy conservation. The temperature and the water vapour mixing ratio are smoothly connected at the tropopause.

## Carbon sequestration

**The alteration of oceanic crust.** The alteration of upper oceanic crust is a major source of carbon entering subduction zones<sup>68,69</sup>, and its flux size is likely to have been larger in the Hadean. The upper 500 m of oceanic crust is highly porous, and considering rapid kinetics under high surface temperatures, the porous layer would have efficiently reacted with the seawater. Under an atmospheric pressure over 100 bar, the solubility of CO<sub>2</sub> in water is elevated by more than an order of magnitude<sup>46</sup>, so reactions between silicates within in the upper oceanic and CO<sub>2</sub> would be promoted as well. Ca and Mg silicates are thermodynamically susceptible to carbonation under a thick CO<sub>2</sub> atmosphere<sup>70</sup>, so we estimate CO<sub>2</sub> uptake by these silicates within in the upper oceanic crust.

The basis for efficient carbonation is that the Hadean seafloor was supersaturated with respect to carbonate minerals. The modern oceans become undersaturated below 3,500–5,000 m<sup>71,72</sup>, but the carbonate compensation depth is likely to have been deeper in the Hadean owing to two main factors<sup>72</sup>: (1) a higher surface temperature due to the greenhouse effect and (2) an initially shallower ocean because of the greater water content of the mantle. The amount of water at the surface is estimated to have been less than 10% of the present day in the Hadean (Fig. 2), so ocean depth is expected to have been shallower than 500 m. Even with an atmospheric pressure of ~200 bar, pressure at the seafloor would be lower than ~250 bar. Higher temperatures and lower pressures inhibit the dissolution of carbonates<sup>72</sup> and thus promote carbonate alteration of the oceanic crust. It is noted that a lower pH due to a thicker CO<sub>2</sub> atmosphere would not be a limiting factor for carbonation. The relative proportion of carbonate ion to the total carbon amount decreases with a lower pH, but carbonate ion concentration would still be larger than the present, or at least remain the same, because the total amount of carbon in the seawater is substantially larger. The actual carbonate ion concentration remains uncertain owing to limited experimental data, but the carbonation of oceanic crust is expected to be efficient as long as carbonate ion is present and dissolution is inhibited.

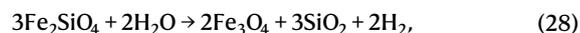
The crust of the chemically heterogeneous mantle would be a mixture of those derived from high-Mg# pyroxenite and Fe-rich blobs, and both components have a large capacity of storing CO<sub>2</sub>. Because the formation of carbonates is thermodynamically favourable for Ca and Mg silicates under a high CO<sub>2</sub> concentration<sup>70</sup>, we assume that all Ca and Mg silicates are used to form carbonates. The crust formed from high-Mg# pyroxenite and Fe-rich blobs both contain ~10 wt% of CaO (Extended Data Table 2), so when all Ca silicates are carbonated, the upper crust would store up to  $3.5 \times 10^{19}$  kg or ~7 bar of CO<sub>2</sub>. This is 2.7 times that of the present-day Earth, where the top 500 m of basaltic crust contains ~3.0 wt% of CO<sub>2</sub>, equivalent to  $1.3 \times 10^{19}$  kg or ~2.5 bar of CO<sub>2</sub><sup>47</sup>. Mg silicates, which mostly exist as olivine, orthopyroxene or clinopyroxene (Extended Data Table 2), are also prone to carbonation<sup>73</sup>, among which olivine has the highest rate of carbonation. The crust of the heterogeneous mantle contains 16–22% of MgO, depending on the relative proportion of high-Mg# and Fe-rich source crusts, so even with a lower bound estimate, the upper crust could contain up to  $8.0 \times 10^{19}$  kg or ~15.4 bar of CO<sub>2</sub>. This suggests that the seafloor could contain up to ~22 bar of CO<sub>2</sub> at one time. Fe silicates are not considered as a sink for CO<sub>2</sub> because they are more likely to be oxidized to produce H<sub>2</sub>.

Carbonates created by hydrothermal alteration would mostly be delivered to the deep mantle under a rapid plate motion. The loss of carbonates in the plate is determined by two factors: (1) the stability of carbonates under a hotter deeper region and (2) the solubility of carbon to water released from the decomposition of hydrous minerals<sup>69</sup>. The stability of carbonates within oceanic crust depends on the *P–T* path of subducting plates, and carbonates are considered to be stable under majority of the modern subduction settings<sup>68</sup>. This is also likely to be the case for the Hadean subduction zones. Although the surface temperature and mantle potential temperature are both

hotter by ~200 K, the *P–T* path of subducting slab would remain similar to the present-day young subduction zones (Extended Data Fig. 3). For the chemically heterogeneous mantle, the rapid plate velocity would allow the slab to be delivered to the deeper region without substantial heating from the surrounding mantle. A pyrolytic homogeneous mantle would have slower plate velocity, but because oceanic plates are older and thus colder, the slab temperature at the deeper region would be similar to that of the heterogeneous mantle. The actual geotherm could vary among different subduction settings even with the same age and plate velocity<sup>74</sup>, so the temperature of some slab surfaces may reach the solidus of carbonate melting<sup>75</sup>. On average, however, the subducting slab is expected to remain colder than the carbonate solidus (Extended Data Fig. 3), recycling only a fraction of subducting carbonates back to the surface. Moreover, some fraction of the extracted carbon would be stored in mantle lithosphere and continental crust<sup>69</sup>, the latter of which would have been created by the melting of hydrated subducted materials. Modelling the thermal structure of subduction zones is still subject to large uncertainties as a number of important assumptions are involved, and in this study, we tentatively estimate that 50% of subducted carbonates return to the surface for both pyrolytic and heterogeneous mantles (Fig. 4). Whereas the timescale of carbon sequestration would be longer for less efficient carbon subduction, it would always be shorter by an order of magnitude for the case of the heterogeneous mantle.

The loss of carbon may also take place by the dissolution of carbonates to fluid released by serpentine. The Hadean plates, however, are expected to contain ~9 times more carbonates than the present-day oceanic crust, and thus it is unlikely for all carbonates to be dissolved. When the top 500 m of oceanic crust contains ~10 wt% of water, the maximum amount of CO<sub>2</sub> that could dissolve into serpentine-driven fluid is  $4.4 \times 10^{17}$  kg for every surface renewal cycle, which is less than 1% of total carbonates in oceanic crust. Here we assume that serpentine releases water at ~3 GPa and the solubility of carbonates to fluid is 10<sup>4</sup> ppm<sup>69</sup>. The amount of water in the underlying crust and mantle is predicted to be limited, owing to high confining pressure<sup>76,77</sup>. Considering that the top 30 km includes 0.1 wt% of water, the additional dissolution of CO<sub>2</sub> would be less than 1% of total carbonates in the upper crust. Therefore, the amount of recycled carbon through dissolution is expected to be negligible in the Hadean.

**The composition and redox of the atmosphere.** For both chemically homogeneous and heterogeneous mantles, crust has a higher MgO content and thus forms more olivine than the present-day oceanic crust. The dissolution of olivine is efficient compared to other silicate minerals, and thus the following reactions are likely to occur:



where each reaction represents oxidation of ferrous iron and serpentinization of forsterite. We assume that all fayalite would be oxidized to form magnetite by reaction (28). The serpentinization of forsterite would consume SiO<sub>2</sub> and thus promotes the oxidation of iron and the carbonation of other minerals.

The amount of hydrogen production differs between the chemically homogeneous and heterogeneous mantles because of their difference in mineral assemblage of the seafloor. Crust with a lower Mg# contains more iron and thus produces more H<sub>2</sub>. Following the stoichiometry of reactions, 0.07 mol of H<sub>2</sub> is estimated to be released to the atmosphere per 1 mol of olivine in the case of the homogeneous pyrolytic mantle, whereas 0.04 mol of H<sub>2</sub> is released for the high-Mg# crust of the chemically heterogeneous mantle. The H<sub>2</sub> production rate, however, is higher for the chemically heterogeneous mantle because the seafloor is renewed at a rate ~10 times faster than the homogeneous pyrolytic mantle (Fig. 4a).

The composition of the atmosphere is calculated using Gibbs free-energy minimization, the implementation of which is described in ref. <sup>78</sup>. We calculate equilibrium under temperature and pressure conditions at the bottom of the atmosphere. CO<sub>2</sub>, CO, CH<sub>4</sub>, H<sub>2</sub>O and H<sub>2</sub> are considered as possible species. In reality, the atmospheric composition is affected by photochemical reactions. Such an effect, however, is not included because our aim is to provide a zeroth-order estimate on the change in redox state with active carbonation and serpentinization.

**Subduction geotherms.** The  $P$ – $T$  path of Extended Data Fig. 3 is calculated using the model of ref. <sup>79</sup>. The age of subducting plate is assumed to be 10 Myr with a slab dip angle of 45°, but the angle does not have a substantial influence on the geotherm. For an activation energy for viscosity, the value of 300 kJ mol<sup>-1</sup> is adopted. Because the model assumes an incompressible fluid, the modelled potential temperature is converted to the actual value using an adiabatic gradient of 0.5 K km<sup>-1</sup>.

## Data availability

All relevant data are provided in the paper. Codes to reproduce the results are available at <https://github.com/yoshi-miyazaki/Hadean-evolution/>. The Gibbs energy minimization code is available at <https://github.com/yoshi-miyazaki/GibbsE-minimization/>. Source data are provided with this paper.

52. Zahnle, K. J., Kasting, J. F. & Pollack, J. B. Evolution of a steam atmosphere during Earth's accretion. *Icarus* **74**, 62–97 (1988).
53. Dullien, F. A. L. Porous Media: Fluid Transport and Pore Structure 2nd edn (Academic, 1992).
54. Zahnle, K. J., Lupu, R., Dobrovolskis, A. & Sleep, N. H. The tethered Moon. *Earth Planet. Sci. Lett.* **427**, 74–82 (2015).
55. Trønnes, R. G. & Frost, D. J. Peridotite melting and mineral-melt partitioning of major and minor elements at 22–24.5 GPa. *Earth Planet. Sci. Lett.* **197**, 117–131 (2002).
56. Corgne, A., Liebske, C., Wood, B. J., Rubie, D. C. & Frost, D. J. Silicate perovskite-melt partitioning of trace elements and geochemical signature of a deep perovskitic reservoir. *Geochim. Cosmochim. Acta* **69**, 485–496 (2005).
57. Parsons, B. Causes and consequences of the relation between area and age of the ocean floor. *J. Geophys. Res.* **87**, 289–302 (1982).
58. Zhang, G., Mei, S. & Song, M. Effect of water on the dislocation creep of enstatite aggregates at 300 MPa. *Geophys. Res. Lett.* **47**, e2019GL085895 (2020).
59. Aubaud, C., Hauri, E. H. & Hirschmann, M. M. Hydrogen partition coefficients between nominally anhydrous minerals and basaltic melts. *Geophys. Res. Lett.* **31**, L20611 (2004).
60. de Capitani, C. & Petrakakis, K. The computation of equilibrium assemblage diagrams with Theriak/Domino software. *Am. Mineral.* **95**, 1006–1016 (2010).
61. McKenzie, D. The generation and compaction of partially molten rock. *J. Petrol.* **25**, 713–765 (1984).
62. Christensen, U. R. Thermal evolution models for the Earth. *J. Geophys. Res.* **90**, 2995–3007 (1985).
63. Korenaga, J. Thermal cracking and the deep hydration of oceanic lithosphere: A key to the generation of plate tectonics? *J. Geophys. Res.* **112**, B05408 (2007).
64. Tackley, P. J. In *Treatise on Geophysics: Volume 7: Mantle Dynamics* 2nd edn (ed. Schubert G.) 521–585 (Elsevier, 2015).
65. Nakajima, S., Hayashi, Y.-Y. & Abe, Y. A study on the “runaway greenhouse effect” with a one-dimensional radiative–convective equilibrium model. *J. Atmos. Sci.* **49**, 2256–2266 (1992).
66. Johnson, S. S., Mischna, M. A., Grove, T. L. & Zuber, M. T. Sulfur-induced greenhouse warming on early Mars. *J. Geophys. Res. Planet.* **113**, E08005 (2008).
67. Abe, Y. & Matsui, T. The formation of an impact-generated H<sub>2</sub>O atmosphere and its implications for the early thermal history of the Earth. *J. Geophys. Res. Suppl.* **90**, C545–C559 (1985).
68. Dasgupta, R. & Hirschmann, M. M. The deep carbon cycle and melting in Earth's interior. *Earth Planet. Sci. Lett.* **298**, 1–13 (2010).
69. Kelemen, P. B. & Manning, C. E. Reevaluating carbon fluxes in subduction zones, what goes down, mostly comes up. *Proc. Natl Acad. Sci.* **112**, E3997–E4006 (2015).
70. Sleep, N. H., Zahnle, K. & Neuhoff, P. S. Initiation of clement surface conditions on the earliest Earth. *Proc. Natl Acad. Sci.* **98**, 3666–3672 (2001).
71. Peterson, M. N. A. Calcite: rates of dissolution in a vertical profile in the central Pacific. *Science* **154**, 1542–1544 (1966).
72. Andersson, A. J. In *Treatise on Geochemistry. Volume 8: The Oceans and Marine Geochemistry* 2nd edn (eds Holland, H. D. & Turekian, K.) 519–542 (Elsevier, 2014).
73. Kelemen, P. B. et al. Rates and mechanisms of mineral carbonation in peridotite: natural processes and recipes for enhanced, in situ CO<sub>2</sub> capture and storage. *Annu. Rev. Earth Planet. Sci.* **39**, 545–576 (2011).
74. Syracuse, E. M., van Keken, P. E. & Abers, G. A. The global range of subduction zone thermal models. *Phys. Earth Planet. Inter.* **183**, 73–90 (2010).
75. Dasgupta, R., Hirschmann, M. M. & Withers, A. C. Deep global cycling of carbon constrained by the solidus of anhydrous, carbonated eclogite under upper mantle conditions. *Earth Planet. Sci. Lett.* **227**, 73–85 (2004).
76. Korenaga, J. On the extent of mantle hydration caused by plate bending. *Earth Planet. Sci. Lett.* **457**, 1–9 (2017).
77. Miller, N. C., Lizarralde, D., Collins, J. A., Holbrook, W. S. & Van Avendonk, H. J. Limited mantle hydration by bending faults at the middle America trench. *J. Geophys. Res. Solid Earth* **126**, e2020JB020982 (2021).
78. Miyazaki, Y. & Korenaga, J. Effects of chemistry on vertical dust motion in early protoplanetary disks. *Astrophys. J.* **849**, 41 (2017).
79. Wirth, E. A. & Korenaga, J. Small-scale convection in the subduction zone mantle wedge. *Earth Planet. Sci. Lett.* **357–358**, 111–118 (2012).
80. Lyubetskaya, T. & Korenaga, J. Chemical composition of Earth's primitive mantle and its variance: 1. Method and results. *J. Geophys. Res.* **112**, B03211 (2007).
81. Gale, A., Dalton, C. A., Langmuir, C. H., Su, Y. & Schilling, J.-G. The mean composition of ocean ridge basalts. *Geochem. Geophys. Geosyst.* **14**, 489–518 (2013).

**Acknowledgements** This work was sponsored by the US National Aeronautics and Space Administration under Cooperative Agreement No. 80NSSC19M0069 issued through the Science Mission Directorate and the National Science Foundation under grant EAR-1753916. This work was also supported in part by the facilities and staff of the Yale University Faculty of Arts and Sciences High Performance Computing Center. Y.M. was supported by the Stanback Postdoctoral Fellowship from Caltech Center for Comparative Planetary Evolution. The authors thank N. Sleep and M. Hirschmann for providing constructive comments, which were helpful to substantially improve the accuracy of the manuscript.

**Author contributions** Y.M. and J.K. designed the study, discussed the results, and wrote the manuscript. Y.M. performed calculations.

**Competing interests** The authors declare no competing financial interests.

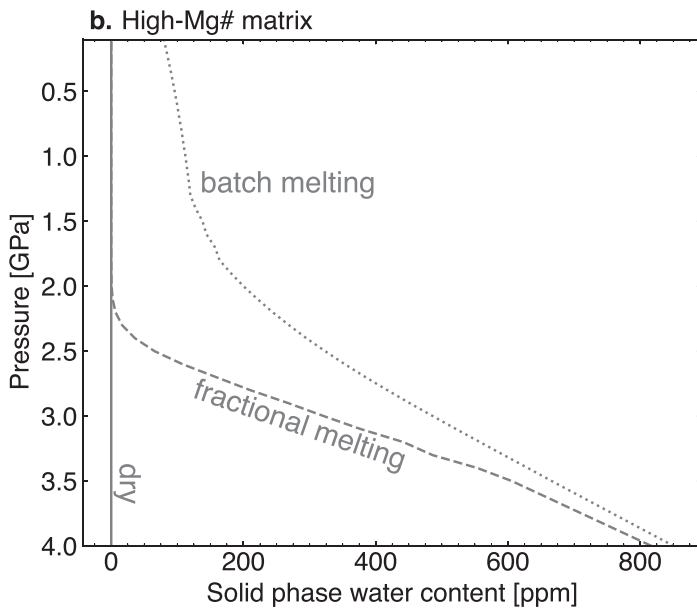
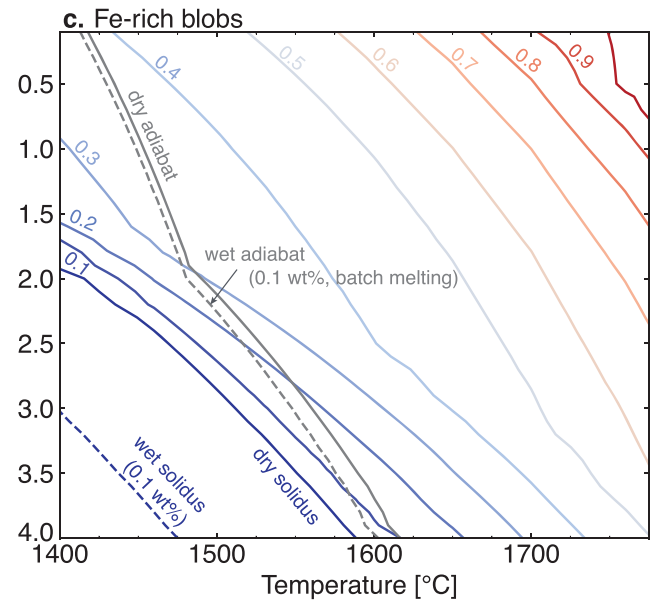
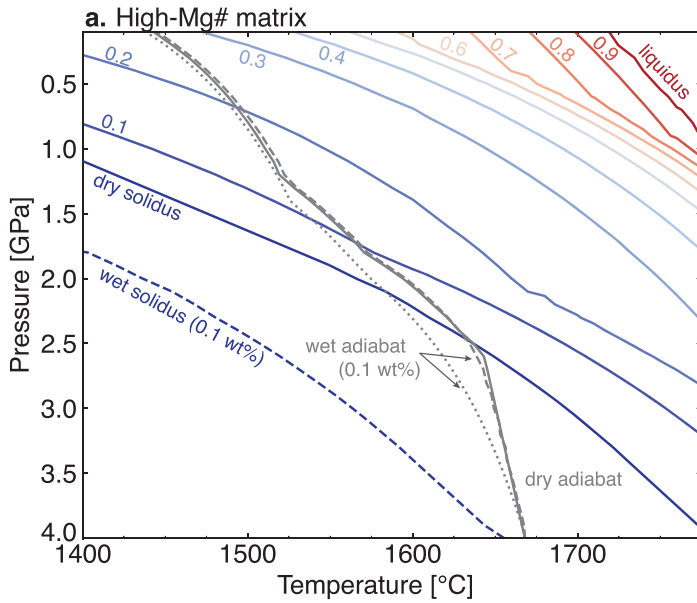
## Additional information

**Supplementary information** The online version contains supplementary material available at <https://doi.org/10.1038/s41586-021-04371-9>.

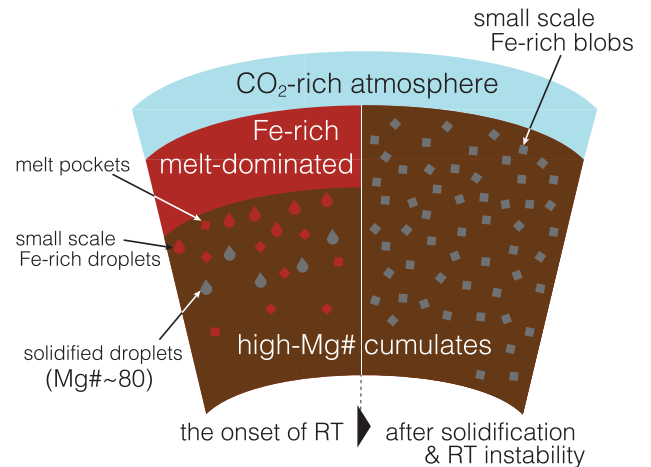
**Correspondence and requests for materials** should be addressed to Yoshinori Miyazaki.

**Peer review information** Nature thanks Marc Hirschmann and Norman Sleep for their contribution to the peer review of this work. Peer reviewer reports are available.

**Reprints and permissions information** is available at <http://www.nature.com/reprints>.



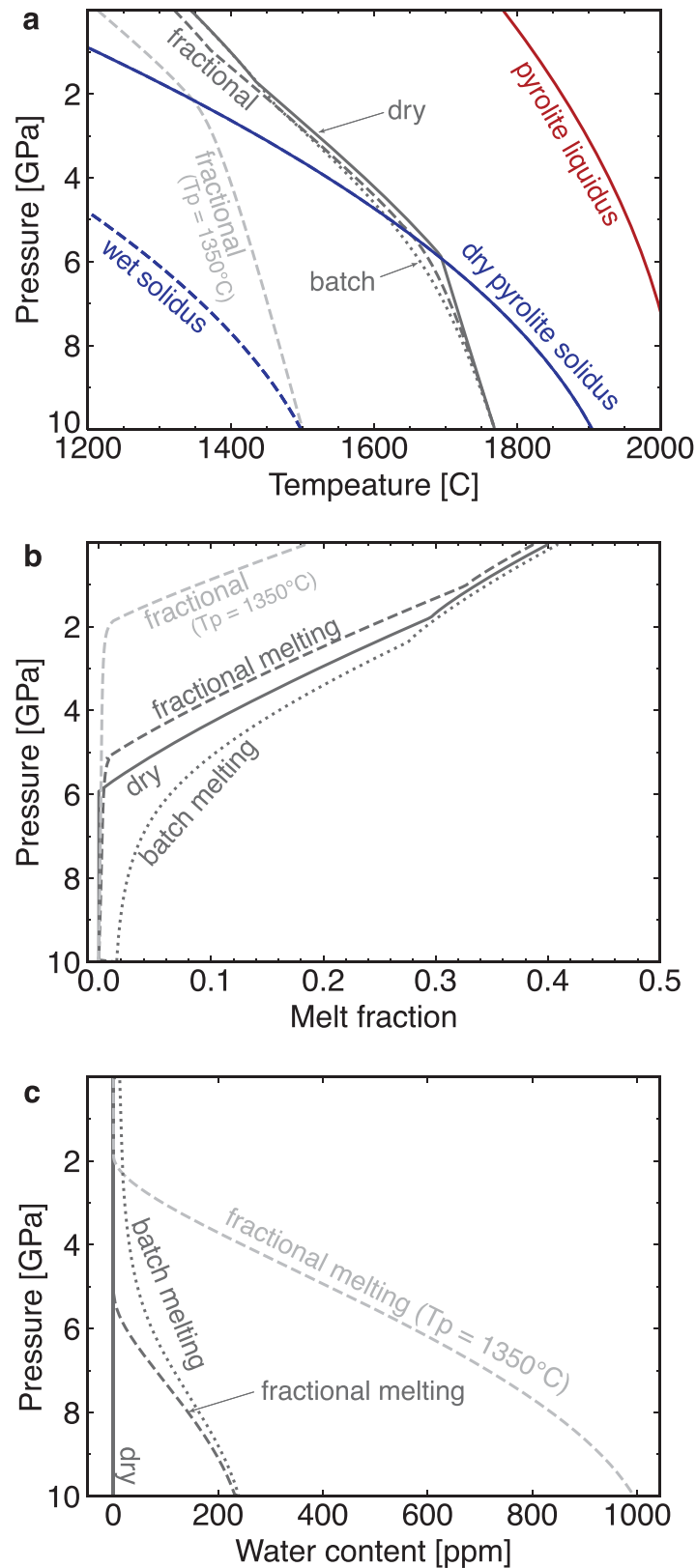
**d. The formation of heterogeneous mantle**



**Extended Data Fig. 1 | The thermal structure of the chemically heterogeneous mantle plotted together with contours of melt fraction.**

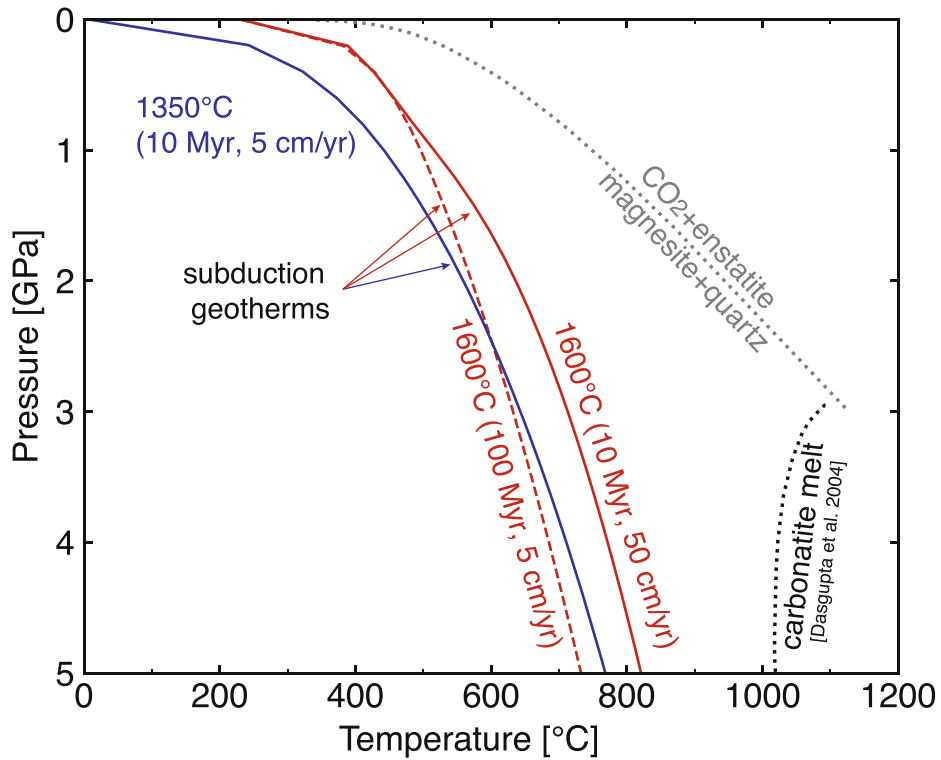
**a–c,** Melt fraction is shown for two components of the mantle: high-Mg# pyroxenite matrix (**a**) and Fe-rich blobs (**c**), and water content remaining in the solid phase of the high-Mg# matrix (**b**). The melt fractions of high-Mg# matrix and Fe-rich blobs are estimated using the Rhyolite-MELTS model<sup>42</sup>. The dry (grey solid) and wet (0.1 wt%; grey dashed) adiabats are calculated with a potential temperature of 1,600 °C, using equation (17). For the wet adiabat of the high-Mg# matrix, two modes of melting are considered, batch (dotted) and fractional (dashed), and for the latter, we assume that 90% of melt would escape from the mantle for every 0.1 GPa of ascent when the degree of melting is greater than 1%. The fraction of melt escaping the system is insensitive to the

thickness of complete dehydration, and values between 10% and 99.9% would yield a thickness within 0.1 GPa of what is predicted in this figure. **d,** Schematic illustration of the compositional structure of the mantle during and after the solidification of a magma ocean under fractional crystallization. The mantle experiences global-scale chemical stratification, leaving an Fe-rich layer near the surface. Such stratification is subject to the Rayleigh–Taylor (RT) instability, resulting in the dripping-like descent of Fe-rich materials. This period corresponds to Fig. 1a. These droplets would solidify as they sink through the mantle (left) and be mixed with high-Mg# cumulates. When the surface becomes rheologically solid (Fig. 1b), the mantle would have a structure with small-scale chemical heterogeneity, embedded in high-Mg# matrix (right).



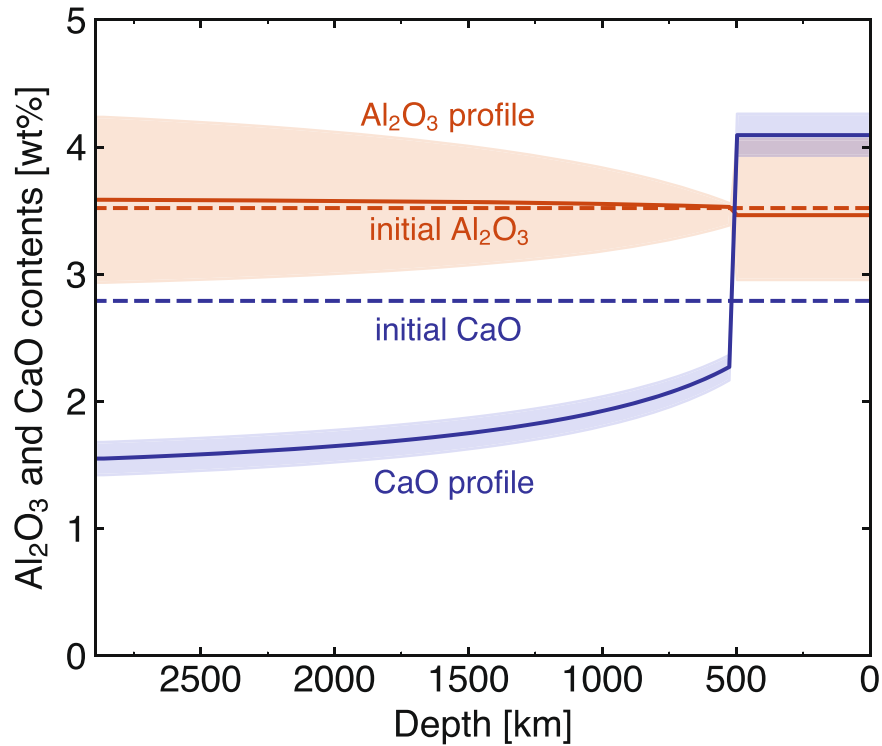
**Extended Data Fig. 2 | Thermal structure of a pyrolitic (chemically homogeneous) mantle when a melt-dominated layer disappears.** The figure describes when the entire mantle starts to behave rheologically as solid, which corresponds to a potential temperature of  $-1,600\text{ }^{\circ}\text{C}$ . **a–c**, The profiles of temperature (**a**), melt fraction (**b**) and water content (**c**) are shown for both dry (grey solid) and wet (0.1 wt%; grey dotted and dashed) mantles, together with the solidus (blue) and liquidus of pyrolite (red). The solidus of a wet mantle (blue dashed) is estimated using equation (18) and a melt/mineral partitioning

coefficient of  $D = 0.005$ . Two modes of melting are considered for the wet mantle, batch (dotted) and fractional (dashed). Temperature profiles would be adiabatic as a result of the Rayleigh–Taylor instability, and melt fraction is estimated using a model of ref. <sup>24</sup> with the mass fraction of clinopyroxene of 19 wt%. For fractional melting, we assume that 90% of melt would escape from the mantle for every 0.1 GPa of ascent when the degree of melting is greater than 1%.



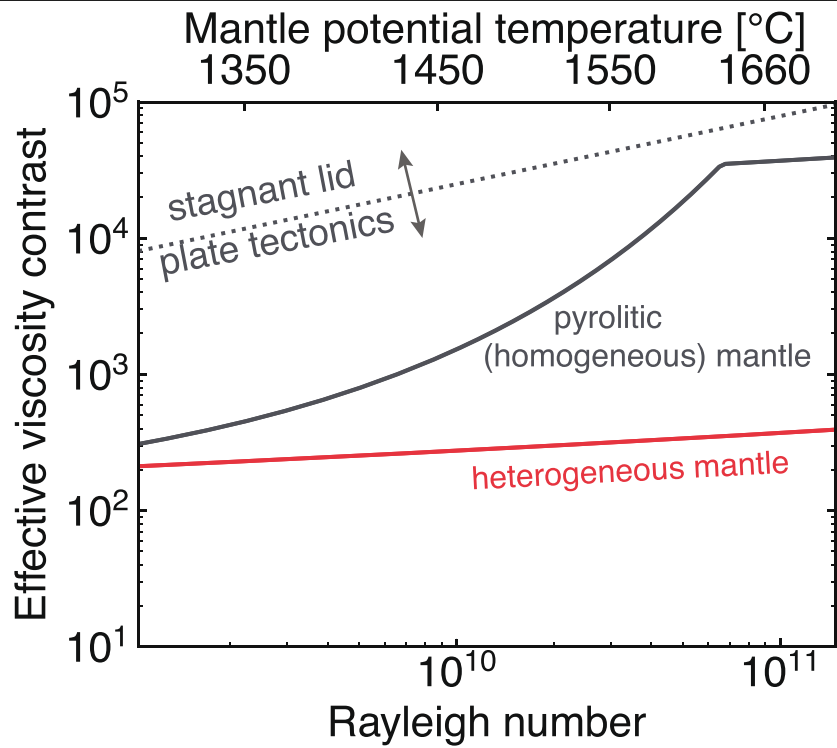
**Extended Data Fig. 3 | The subduction geotherm during the Hadean with the stability field of carbonates.**  $P$ - $T$  paths are calculated assuming a dip angle of  $45^\circ$  using the model of ref.<sup>79</sup> (see Methods for details). We consider (1) a mantle potential temperature of  $1,350^\circ\text{C}$  with a plate age of 10 Myr, a velocity of  $5\text{ cm yr}^{-1}$ , and a surface temperature of  $0^\circ\text{C}$  (blue), (2) a potential temperature of  $1,600^\circ\text{C}$  with a plate age of 10 Myr, a velocity of  $50\text{ cm yr}^{-1}$ , and a surface temperature of  $230^\circ\text{C}$  (red solid), and (3) a potential temperature of  $1,600^\circ\text{C}$  with a plate age of 100 Myr, a velocity of  $5\text{ cm yr}^{-1}$ , and a surface temperature of

$230^\circ\text{C}$  (red dashed), representing the present-day young slab, the Hadean slab of the chemically heterogeneous mantle, and that of a homogeneous pyrolitic mantle, respectively.  $P$ - $T$  paths of the heterogeneous and homogeneous mantles are similar because rapid plate motion mitigates the heating of the slab from the surrounding mantle. The solidus of carbonate melt is adopted from ref.<sup>75</sup> (black dotted), and the decomposition of magnesite under the presence of quartz is calculated using Theriak-Domino<sup>60</sup> (grey dotted).



**Extended Data Fig. 4 | The profiles of Al<sub>2</sub>O<sub>3</sub> (red) and CaO (blue) contents after magma ocean solidification.** Profiles before the onset of small-scale Rayleigh-Taylor instabilities are shown. The top 500 km of the mantle becomes the source for iron-rich blobs, whereas the lower mantle composition corresponds to the high-Mg# matrix in the main text. We assume that newly formed crystals in the magma ocean would stack at the base of the melt-dominated layer (Fig. 1a). Initial

concentrations of Al<sub>2</sub>O<sub>3</sub> 3.5 wt% and CaO 2.8 wt%<sup>80</sup> are assumed (dashed lines), and partitioning coefficients between melt and bridgmanite are calculated from the experimental results of Trønnes and Frost<sup>55</sup> and Corgne et al.<sup>56</sup>. Shaded areas represent uncertainties, which are calculated using partitioning coefficients 30% larger and smaller values than the mean estimated values ( $D_{Al/Si} = 0.78$  and  $D_{Ca/Si} = 0.16$ ).



**Extended Data Fig. 5 | Effective viscosity contrast across the lithosphere and the criteria for plate tectonics.** Effective viscosity contrast is shown (equation (14)) as a function of the internal Rayleigh number, together with the corresponding mantle potential temperature. The thickness of depleted

lithospheric mantle  $h_m$  in equation (14) is different between chemically homogeneous (grey) and heterogeneous mantles (red), and the values of  $h_m$  are shown in Fig. 3b. The criteria for plate tectonics ( $\Delta\eta_{L,crit}$  in equation (20)) is also plotted with a dotted line.

# Article

Extended Data Table 1 | The evolution of CO<sub>2</sub> and H<sub>2</sub>O budgets

	CO <sub>2</sub> [kg]		H <sub>2</sub> O [kg]	
	surface	interior	surface	interior
After the Giant Impact	$9.0 \times 10^{20}$	$3.0 \times 10^{20}$	$4.6 \times 10^{19}$	$4.0 \times 10^{21}$
After the solidification of mantle surface	$9.3 \times 10^{20}$	$2.7 \times 10^{20}$	$1.1 \times 10^{20}$	$3.9 \times 10^{21}$
The end of Hadean	$1.7 \times 10^{19}$	$1.2 \times 10^{21}$	$4.2 \times 10^{21}$	0
Present-day	$1.7 \times 10^{17}$	$1.2 \times 10^{21}$	$1.4 \times 10^{21}$	$2.8 \times 10^{21}$

The initial CO<sub>2</sub> and H<sub>2</sub>O concentrations are set to 300ppm and 0.1wt%, respectively, to calculate these values. Estimates for the magma ocean stage are taken from Fig. 2, which is calculated based on the volatile partitioning model. Because of rapid plate tectonics, most CO<sub>2</sub> in the atmosphere was sequestered to the mantle, whereas remaining water in the mantle was degassed by the end of the Hadean (see Methods for details). The present-day values are adopted from refs.<sup>25,26</sup>.

**Extended Data Table 2 | Compositions of high-Mg# pyroxenite, iron-rich blobs and their differentiated components**

	Oxide composition [wt%]					Mineral composition [wt%]					density [kg/m <sup>3</sup> ]
	SiO <sub>2</sub>	MgO	FeO	Al <sub>2</sub> O <sub>3</sub>	CaO	olivine	opx	cpx	feldspar	others	
High-Mg# crust*	43.6	21.5	5.3	18.9	10.7	20.9	21.5	26.9	18.5	12.1 <sup>§</sup>	3010 <sup>#</sup>
High-Mg# DLM	52.0	41.5	4.2	1.8	0.5	33.4	64.7	1.9	-	-	3120
High-Mg# pyroxenite	51.3	39.5	4.1	3.5	1.5	24.9	69.8	-	-	5.2 <sup>§</sup>	3130
Iron-rich crust <sup>†</sup>	39.2	16.0	22.9	9.2	12.6	38.9	-	46.3	1.5	13.4 <sup>  </sup>	3570 <sup>☆</sup>
Iron-rich DLM	33.9	45.5	18.1	1.61	1.02	85.2	-	-	-	14.8 <sup>  </sup>	3340
Iron-rich blobs	35.3	37.8	19.0	3.7	4.1	84.0	-	-	-	16.0 <sup>  </sup>	3350
Modern MORB <sup>‡</sup>	50.47	7.58	10.43	14.7	9.4	9.3	11.6	24.1	51.4	3.5 <sup>¶</sup>	3030

Mineral proportions and densities are calculated using Theriak-Domino<sup>60</sup> under 250 °C and 10 bar for crustal components and 1,500 °C and 1.2 GPa for mantle components. DLM indicates depleted lithospheric mantle, which is calculated as the depleted residue of partial melting.

\*From the partial melt of pyroxenite at 1,570 °C and 1.8 GPa with 11% melting.

†From the partial melt of iron-rich blob at 1,520 °C and 2.3 GPa with 28 wt% melting.

‡From ref.<sup>81</sup>. The total of oxides is lower than 100% because other minor oxides, including Na<sub>2</sub>O and TiO<sub>2</sub>, are not shown here.

§The high-Mg# pyroxenite contains spinel, whereas crust contains corundum.

||Iron-rich blobs and its depleted reservoir include merwinite, spinel, and periclase, whereas iron-rich crust only contains spinel.

¶Mid-ocean ridge basalt contains ilmenite as a Ti-bearing phase.

☆Before crystallization, the melt density of partial melt from the high-Mg# pyroxenite is 2,660 kg m<sup>-3</sup>. The melt density is calculated using the Rhyolite-MELTS model<sup>42</sup> at a temperature of 1,500 °C and 10 bar. Under a mantle condition of 1,500 °C and 1.2 GPa, the density increases to 3,180 kg m<sup>-3</sup>, and it is likely to be heavier than the ambient mantle.

☆Before crystallization, the melt density of partial melt from iron-rich blobs is 3,000 kg m<sup>-3</sup>. The melt would thus migrate upwards within the pyroxenite matrix. Its density under the mantle condition is estimated to be 3,440 kg m<sup>-3</sup>.